Chem Soc Rev

Uphill Diffusion in Multicomponent Mixtures

Journal:	*Chemical Society Reviews*
Manuscript ID:	CS-TRV-12-2014-000440.R1
Article Type:	Tutorial Review
Date Submitted by the Author:	22-Feb-2015
Complete List of Authors:	Krishna, Rajamani; University of Amsterdam, Van 't Hoff Institute for Molecular Sciences

Uphill Diffusion in Multicomponent Mixtures

Rajamani Krishna

Footnotes

Van 't Hoff Institute for Molecular Sciences, University of Amsterdam, Science Park 904, 1098 XH Amsterdam, The Netherlands. Fax: 31 20 525 5604; Tel: 31 20 627 0990; E-mail: r.krishna@contact.uva.nl

† Electronic Supplementary Information (ESI) available: This material provides (a) Detailed derivation of the Maxwell-Stefan and Onsager formulations for describing mixture diffusion, (b) Procedure for estimations of diffusivities, (c) Simulation details, and methodologies for transient equilibration, along with input parameters, and (d) video animations highlighting the motion of molecules with zeolites, and transient uptake within crystals. See DOI: 10.1039/b000000x/

Key Learning Points

1. Coupling effects in mixture diffusion may cause uphill transport of a component
2. Uphill diffusion results in transient overshoots and serpentine equilibration trajectories
3. Phase equilibrium thermodynamics is often the major source of diffusional coupling effects
4. Chemical potential gradients are the proper driving forces for diffusion
5. Uphill transport can be exploited to achieve difficult and unusual separations

ABSTRACT

Molecular diffusion is an omnipresent phenomena that is important in a wide variety of contexts in chemical, physical, and biological processes. In the majority of cases, the diffusion process can be adequately described by Fick's law that postulates a linear relation between the flux of any species and its own concentration gradient. Most commonly, a component diffuses down the concentration gradient. The major objective of this review is to highlight a very wide variety of situations that cause uphill transport of one constituent in the mixture.

Uphill diffusion may occur in multicomponent mixtures in which the diffusion flux of any species is strongly coupled to that of partner species. Such coupling effects often arise from strong thermodynamic non-idealities; for a quantitative description we need to use chemical potential gradients as driving forces. The transport of ionic species in aqueous solutions is coupled with its partner ions because of the electro-neutrality constraints; such constraints may accelerate or decelerate a specific ion. When uphill diffusion occurs, we observe transient overshoots during equilibration; the equilibration process follows serpentine trajectories in composition space. For mixtures of liquids, alloys, ceramics and glasses the serpentine trajectories could cause entry into meta-stable composition zones; such entry could result in phenomena such as spinodal decomposition, spontaneous emulsification, and the Ouzo effect.

For distillation of multicomponent mixtures that form azeotropes, uphill diffusion may allow crossing of distillation boundaries that are normally forbidden. For mixture separations with microporous adsorbents, uphill diffusion can cause supra-equilibrium loadings to be achieved during transient uptake within crystals; this allows the possibility of over-riding adsorption equilibrium for achieving difficult separations.

1. Introduction

The quantitative description of diffusion of mixtures of molecules is important to chemists, physicists, biologists, and engineers in a variety of disciplines and applications.[1-4] For a binary mixture of components 1 and 2, the flux of component 1 with respect to the molar average velocity of the mixture, J_1, is commonly related to its composition (mole fraction) gradient in the form

$$J_1 = -c_t D_{12}\left(dx_1/dz\right) \tag{1}$$

The linear relation (1) was posited in 1855 by Adolf Fick, a physiologist working as an anatomy demonstrator in Zürich, in analogy to the corresponding laws of conduction of heat and electricity. The coefficient D_{12} in Equation (1) is the Fick diffusivity, and c_t is the total molar concentration of the mixture. Since the mole fractions sum to unity, there is only one independent composition gradient. Unless $D_{12} < 0$, the flux J_1 is directed downhill; this implies that the flux J_1 has the same sign as $-dx_1/dz$, as pictured in Figure 1a. The simplest extension of Equation (1) to *n*-component mixtures is to postulate that each flux is dependent on its own composition gradient

$$J_i = -c_t D_i\left(dx_i/dz\right); \quad i = 1,2,...n \tag{2}$$

where D_i is the "effective" Fick diffusivity of component *i*.

To set the scene for this tutorial, let us examine four sets of data on mixture diffusion: (a) in the gas phase, (b) between two partially miscible liquid phases, (c) in a solid metal phase, and (d) within a microporous crystalline material.

The experimental data of Duncan and Toor[5] on transient approach to equilibrium of $H_2(1)/N_2(2)/CO_2(3)$ gas mixtures of two different compositions in Bulb A and Bulb B, connected by a capillary, are shown in Figures 1b, c, and d. Let us first examine the equilibration of H_2, and CO_2. The

composition - time trajectories are as expected; H_2 diffuses from Bulb B to Bulb A and the two composition sets approach each other as time progresses. CO_2 diffuses from Bulb A to Bulb B in the expected, normal, fashion. The diffusion behavior of these two species H_2, and CO_2 may be termed as Fickian, i.e. down their respective composition gradients.

The composition - time trajectory of N_2 displays several curious phenomena. Initially, the compositions of nitrogen in the two bulbs are almost identical and therefore at the start of the experiment, the composition gradient driving force for N_2 is practically zero. However, diffusion of N_2 does take place, decreasing the composition of Bulb A; concomitantly the composition of Bulb B increases. This is contrary to the Fickian expectations for we have $dx_2/dz \approx 0; \quad J_2 \neq 0; \quad t \approx 0$. The composition of nitrogen in Bulb A continues to decrease during the time interval $0 < t < t_1$, where $t_1 \approx 6$ h; diffusion of nitrogen is up-hill, i.e. $J_2/(-dx_2/dz) < 0; \quad 0 < t < t_1$. Uphill diffusion of N_2 continues to take place until the time $t = t_1$ is reached, when the composition profiles in both bulbs tend to plateau. The plateau implies that the diffusion flux of N_2 is zero, despite the existence of a large driving force. At $t = t_1$ we have $dx_2/dz \neq 0; \quad J_2 = 0; \quad t = t_1$. Beyond the point $t = t_1$, the diffusion behavior of N_2 is "normal", i.e. the composition of nitrogen in Bulb B (with a higher composition) decreases while the composition of nitrogen in Bulb A (with the lower composition) increases. The equilibration trajectory follows a serpentine path in composition space (cf. Figure 1d).

In the immersion precipitation process for membrane preparation, a 10% solution of cellulose acetate in acetone is immersed in a bath of pure water.[6] Figure 2 depicts the composition trajectories at three different times, as the mixture reaches the equilibrium state (marked EQ). Outside the binodal envelope, we have homogeneous single phase mixtures. Within the spinodal envelope, the mixture splits into two phases. The region between the binodal and spinodal envelopes is meta-stable. The circuitous path followed at t = 50 s has entered the meta-stable region between the binodal and spinodal envelopes; this foray impacts on the membrane structure and properties.[6]

Figure 3a presents data on inter-diffusion of Fe/Mg/Ca mixtures in garnet, a precious stone consisting of a deep red vitreous silicate mineral.[7] Slabs with two different compositions are brought into contact at time $t = 0$, and the composition profiles on either side of the interface ($z = 0$) are monitored at various time intervals. The composition profiles at $t = 100$ h displays spatial overshoot and undershoot for Mg. In composition space, the equilibration trajectory is serpentine in shape (cf. Figure 3b).

The transient uptake of *n*-hexane(nC6)/2-methylpentane(2MP) mixtures in microporous crystals of MFI zeolite, exposed to an equimolar gas phase mixture at constant total pressure (= 2.6 Pa) is shown in Figure 4.[8] The transient equilibration of nC6 displays a pronounced overshoot, achieving supra-equilibrium loadings during the initial stages.

The four data sets underscore the inadequacies of Equation (2). Using finite and constant values of D_i, no overshoots or undershoots are permitted; the transient equilibration process must follow straight-line trajectories in composition space.

This tutorial review has the following set of objectives.

(1) To consider and discuss flux expressions that adequately describe transient overshoots, and serpentine composition trajectories in mixture diffusion. We shall show that the curious characteristics noted in Figures 1, 2, 3, and 4 are fingerprints of uphill diffusion. This phenomenon is of relevance in a wide variety of processes.

(2) To stress the need for use of the more fundamental chemical potential gradients as driving forces for modelling multicomponent mixture diffusion.

(3) To underscore the possibility that serpentine equilibration trajectories may enter meta-stable composition regions of partially miscible liquid mixtures. This could lead to spontaneous emulsification and the formation of meta-stable dispersions.

(4) To suggest the potential of separating azeotropic mixtures by exploiting uphill transport in distillation, and partial condensation processes.

(5) For separations with microporous crystalline adsorbents, to demonstrate that transient overshoots may be exploited to achieve separations that are infeasible on the basis of adsorption equilibrium alone.

The Electronic Supporting Information (ESI) provides detailed derivations of flux-driving force relations, along with solutions to the model equations describing transient equilibration processes. All the necessary data inputs, diffusivity estimation procedures, and simulation methodologies are provided in the ESI. This should enable the interested reader to reproduce all the calculations and results presented and discussed here. Here, we focus on explaining the underlying physico-chemical phenomena.

2. Diffusion in ternary gas mixtures

For a quantitative description of the Duncan-Toor experimental data in Figure 1, we need to adopt the Maxwell-Stefan (M-S) diffusion formulation, developed independently by James Clerk Maxwell and Josef Stefan about 150 years ago. In their approach, the composition gradients are expressed as linear functions of the fluxes

$$\begin{aligned} -\frac{dx_1}{dz} &= \frac{x_2 J_1 - x_1 J_2}{c_t Đ_{12}} + \frac{x_3 J_1 - x_1 J_3}{c_t Đ_{13}}; \\ -\frac{dx_2}{dz} &= \frac{x_1 J_2 - x_2 J_1}{c_t Đ_{12}} + \frac{x_3 J_2 - x_2 J_3}{c_t Đ_{23}} \end{aligned} \qquad (3)$$

Only two of the fluxes J_i are independent because the diffusion fluxes sum to zero, $J_1 + J_3 + J_3 = 0$. It is noteworthy that Stefan was aware of Maxwell's work, and commented *Das Studium der Maxwell'schen Abhandlung ist nicht leicht*! The M-S equations represent the balance between the driving force of any individual component with the friction experienced with each partner species; the M-S pair diffusivity $Đ_{ij}$ can be interpreted as an inverse drag coefficient. [2, 9]

The M-S diffusivities of the binary pairs $Đ_{12}$, $Đ_{13}$, and $Đ_{23}$ are independent of the gas composition, and this is a persuasive advantage over the alternative Onsager formulation of Irreversible Thermodynamics.[4] Furthermore, any pair $Đ_{ij}$ remains unchanged in a ternary mixture regardless of the

choice of the "third" component. The pair diffusivity $Đ_{ij}$ can be estimated with good accuracy from the kinetic theory of gases. [2]

We can turn Equation (3) inside-out and obtain an explicit expressions for the fluxes as linear functions of the driving forces. For subsequent discussions, it is convenient to use 2-dimensional matrix notation and write

$$\begin{pmatrix} J_1 \\ J_2 \end{pmatrix} = -c_t \begin{bmatrix} D_{11} & D_{12} \\ D_{21} & D_{22} \end{bmatrix} \begin{pmatrix} \frac{dx_1}{dz} \\ \frac{dx_2}{dz} \end{pmatrix} \tag{4}$$

Equation (4) is proper generalization of Fick's law for ternary mixtures. Equation (3) allows the four elements of the matrix [D] to be determined explicitly as functions of the compositions x_i, and the M-S pair diffusivities $Đ_{ij}$:

$$\begin{bmatrix} D_{11} & D_{12} \\ D_{21} & D_{22} \end{bmatrix} = \frac{\begin{bmatrix} Đ_{13}\left(x_1 Đ_{23} + (1-x_1)Đ_{12}\right) & x_1 Đ_{23}\left(Đ_{13} - Đ_{12}\right) \\ x_2 Đ_{13}\left(Đ_{23} - Đ_{12}\right) & Đ_{23}\left(x_2 Đ_{13} + (1-x_2)Đ_{12}\right) \end{bmatrix}}{x_1 Đ_{23} + x_2 Đ_{13} + x_3 Đ_{12}} \tag{5}$$

Equation (5) reveals that the off-diagonal elements D_{12} and D_{21} are proportional to *differences* in the constituent pair diffusivities $Đ_{ij}$, whereas the diagonal elements D_{11} and D_{22} are weighted averages of $Đ_{ij}$. In the special case in which all the constituent pairs have identical diffusivities, equal to say $Đ$, we get $\begin{bmatrix} D_{11} & D_{12} \\ D_{21} & D_{22} \end{bmatrix} = \begin{bmatrix} Đ & 0 \\ 0 & Đ \end{bmatrix}$, and each species will diffuse independently of its partners.

For $H_2(1)/N_2(2)/CO_2(3)$ gas mixture, the M-S diffusivities are $Đ_{12} = 8.33;\quad Đ_{13} = 6.8;\quad Đ_{23} = 1.68$ (units 10^{-5} $m^2\ s^{-1}$). At the final, equilibrated composition in the Duncan-Toor experiments, the elements of [D] can be calculated from equation (5): $[D] = \begin{bmatrix} 7.68 & -0.11 \\ -3.83 & 2.16 \end{bmatrix} \times 10^{-5}$. Particularly noteworthy is the large magnitude of D_{21} in relation to that of the corresponding diagonal element D_{22}. The rationalization of the curious behavior of N_2 observed in

Figure 1 stem from the contribution of $-D_{21}\,dx_1/dz$ to the flux of N_2, J_2; this contribution is additional to the "normal" contribution $-D_{22}\,dx_2/dz$.

Let us estimate the flux of nitrogen. The composition gradients dx_i/dz can be calculated from the differences between the compositions in the two bulbs, $dx_i/dz = \Delta x_i/\delta = \left(x_{i,B} - x_{i,A}\right)/\delta$ where δ is the length of the capillary tube. So, the flux of nitrogen, (component 2) is $J_2 = -c_t\left(-3.83\times\Delta x_1 + 2.16\times\Delta x_2\right)/\delta\times10^{-5}$. Figure 5 presents a plot of the normalized flux of nitrogen as function of Δx_2. Initially, Δx_2 = 0 but the nitrogen flux remains non-zero and equals $-c_t\left(-3.83\times\Delta x_1\right)/\delta\times10^{-5}$. Since the driving force for H_2, Δx_1 = 0.5, this induces a large positive flux for nitrogen, directed from Bulb A to B, causing the nitrogen composition in Bulb A to decrease. Between the times t =0 and $t = t_1$= 6 h, the direction of nitrogen transport is against its intrinsic gradient; this is reverse or uphill diffusion. Put simply, N_2 is "dragged" uphill by H_2. Indeed the M-S equation (3) can also be interpreted as a balance between the driving force (left members) and the friction between pairs of species (right member); the factors $1/Đ_{ij}$ may be regarded as "drag coefficients".[2, 9]

At the point $t = t_1$ = 6 h, the compositions of N_2 in both bulbs reach a plateau, and so we have $J_2 = -c_t\left(-3.83\times\Delta x_1 + 2.16\times\Delta x_2\right)/\delta\times10^{-5} = 0$ despite the existence of a significant driving force Δx_2; nitrogen experiences a diffusion "barrier". Beyond the point t > 6 h, the diffusion behavior of nitrogen is "normal".

The continuous solid lines in Figures 1c, d are the simulations of the equilibration trajectories obtained by solving Equation (4) in conjunction with the equations of continuity of mass; details are available in the ESI.

The observed occurrence of uphill diffusion is not a violation of the second law of thermodynamics. The second law requires that the *total* rate of entropy production by *all* diffusing species should be positive definite, i.e. $\sigma = -R\sum_{i=1}^{n} J_i \frac{1}{x_i}\frac{dx_i}{dz} \geq 0$. Any component k in the mixture may *consume* entropy

by diffusing uphill, i.e. $-J_k/(dx_k/dz) < 0$, provided the partner components in the mixture *produce* entropy at such a rate that the overall rate of entropy production σ remains positive definite. In the Duncan-Toor[5] experiments, H_2 and CO_2 pump N_2 uphill during the period $0 < t < 6$ h.

Arnold and Toor[10] report experimental data on the transient equilibration of $CH_4(1)/Ar(2)/H_2(3)$ gas mixtures of two different compositions in the top and bottom compartments of a Loschmidt tube; see Figure 6a. The driving forces for the three components are: $\Delta x_1 = -0.515$; $\Delta x_2 = 0.024$; $\Delta x_3 = 0.491$. We note that the driving force for Ar is significantly lower than that of its two partners. The equilibration of CH_4, and H_2 occurs "normally", and monotonously. The equilibration of Ar, however, shows an overshoot (in bottom compartment) and an undershoot (in top compartment). In the ternary composition space, the equilibration follows a serpentine trajectory (cf. Figure 6b). The use of the flux relations (4) with the diffusivity values $[D] = \begin{bmatrix} 4.44 & 1.83 \\ -3.64 & 6.3 \end{bmatrix} \times 10^{-5}$, calculated at the equilibrated compositions using Equation (5), provides a near-quantitative description of the observed trajectories. In these experiments, Ar is dragged uphill by its partner H_2.

Within lung airways, normally at least four gases are involved: O_2, CO_2, N_2 and H_2O; the M-S equation (3) is commonly used to model pulmonary gas transport.[11] The transport of the fresh breathed-in air towards the acini of human beings with chronic obstructive bronchopneumopathy, such as asthma, is rendered difficult due to bronchoconstriction and other factors.[12, 13] Such patients need some respiratory support to allow the oxygen to be transported through the proximal bronchial tree and then diffused in the distal one. One such support system consists of the inhalation of a mixture of heliox (20% O_2; 80% He), that facilitates the transport of oxygen. Oxygen exhibits an overshoot during transient uptake from heliox into the patient (cf. Figure 7). The overshoot arises because O_2 gets dragged uphill during the early transience; experimental data verifies this O_2 overshoot.[11] Uphill transport is an essential part of the heliox therapy.

If we condense a 2-propanol(1)/water(2) vapor mixture of azeotropic composition, the composition of the condensed liquid will be identical to that in the vapor phase and no separation can be achieved,

because there is no driving force for diffusion of either species. If the condensation of the vapor mixture is conducted in the presence of a third component such as nitrogen, that is inert (i.e. does not condense), the situation changes because we now have to reckon with diffusion in a ternary vapor mixture 2-propanol(1)/water(2)/nitrogen(3); see Figure 8. For 85% inert in the vapor mixture, the Fick diffusivity matrix is $[D]=\begin{bmatrix} 1.06 & -0.065 \\ 0.032 & 2.34 \end{bmatrix}\times 10^{-5}$. The condensation of the vapor mixture will result in a liquid composition that is different from the azeotropic composition; this is due to the higher mobility of water molecules in the vapor phase. The contribution of the cross-term, $D_{21}\Delta x_1$ will serve to enhance the flux of water vapor (component 2). The net result is that the condensate will be higher in water content than the azeotropic composition.[4] There is experimental evidence to confirm that diffusion coupling can be harnessed for separating azeotrope mixtures.[14]

3. Phase stability and diffusion in non-ideal liquid mixtures

The proper description of diffusion trajectories in partially-miscible liquid mixtures is important in the design and development of liquid-liquid extraction and emulsification processes. As illustration, Figure 9 shows the phase equilibrium diagram for water/glycerol/acetone mixtures. Let us bring a glycerol/water mixture of composition A in contact with an acetone/water mixture of composition B. The resulting mixture has the composition M, that falls within the spinodal envelope. This mixture is unstable and will separate into two liquid phases of compositions C and D, that are at the ends of the tie-line; C and D are in thermodynamic equilibrium and lie on the binodal curve. The binodal and spinodal curves converge at the plait point. The separation process of liquid extraction is based on the fact that the equilibrated compositions C and D are different from the corresponding initial compositions A and B. Use of Equation (2), with the assumption $D_1 = D_2 = D_3 = D$, anticipates that the A-C and B-D equilibration trajectories are both linear.[15] The A-C and B-D equilibration trajectories, determined experimentally in a stirred two-compartment Lewis stirred cell, are observed to follow curvilinear paths.[16] Use of Equation (2) cannot accurately model the observed equilibration trajectories.

Whether the equilibration process follows a straight-line path or a serpentine path is of crucial importance if we wish to form meta-stable dispersions. For example, if the equilibration of mixtures E and F were to follow a straight-line path, the entire equilibration process remains in the homogeneous single-phase region. However, if a serpentine path is followed, a foray into the meta-stable region occurs; such a foray may result in spontaneous emulsification,[15] and the "Ouzo" effect,[17-19] as explained hereunder.

The aniseed-based alcoholic beverage variously called Ouzo, Anis del Mono, Pastis, Sambuca, and Raki, consists of a three component mixture of ethanol (≈45 vol%), water (≈55 vol%) and an essential oil called trans-anethol (≈ 0.1%).[17] It is consumed with the addition of five volumes of water to one volume of Ouzo. Diffusion of water into the ethanol/trans-anethol phase results in super-saturation of the oil phase which spontaneously nucleates into tiny droplets.[19] The 1 nm sized droplets scatter light, causing the drink to appear milky white.[17] Vitale and Katz[18] have coined the generic term "Ouzo effect" to describe such a process of creating meta-stable liquid-liquid dispersions. Since no input of mechanical energy is involved, this offers an energy-efficient method of producing nanospheres and nanoparticles.[19]

With above background and motivation, let us see how the diffusion process should be modelled to the required level of accuracy. Unlike the case of ideal gas mixtures, discussed in the foregoing section, non-ideal solution thermodynamics has a strong influence on mixture diffusion in liquids. The thermodynamic influences are particularly strong in the vicinity of phase transition regions. The description of diffusion requires the use of chemical potential gradients as driving forces. For *n*-component liquid mixtures, the M-S Equation (3) can be modified by replacing the mole fraction gradient by the "generalized" driving force $\frac{x_i}{RT}\frac{d\mu_i}{dz}$:

$$-\frac{x_i}{RT}\frac{d\mu_i}{dz} = \sum_{\substack{j=1 \\ j\neq i}}^{n} \frac{x_j J_i - x_i J_j}{c_t Đ_{ij}}; \quad i = 1,2,\ldots n \tag{6}$$

Equation (6) is consistent with the Onsager theory of Irreversible Thermodynamics;[4] the Onsager Reciprocal Relations demand the symmetry $Đ_{ij} = Đ_{ji}$. It is not convenient to work with $(x_i/RT)(d\mu_i/dz)$, so we need to relate these to dx_i/dz, that can be determined from measurements. We introduce the component activities, $a_i = \gamma_i x_i$, where γ_i is the activity coefficient in solution, and write $\frac{x_i}{RT}\frac{d\mu_i}{dz} = x_i\frac{d\ln a_i}{dz} = \frac{1}{\gamma_i}\frac{d(\gamma_i x_i)}{dz}$. We also introduce ($n$-1) × ($n$-1) thermodynamic factors Γ_{ij} defined by $\frac{1}{\gamma_i}\frac{d(\gamma_i x_i)}{dz} = \sum_{j=1}^{n-1}\Gamma_{ij}\frac{dx_j}{dz};\quad \Gamma_{ij} = \delta_{ij} + \frac{x_i}{\gamma_i}\frac{\partial\gamma_i}{\partial x_j}$ which allows us to express the left members of Equation (6) in terms of the mole fraction gradients. The elements Γ_{ij} can be determined from models that describe phase equilibrium thermodynamics.[4] For ideal gas mixtures, $a_i = x_i$, $\Gamma_{ij} = \delta_{ij}$ (Kronecker delta) and Equation (6) simplifies to Equation (3).

For a binary mixture (n =2), we obtain a scalar relation

$$J_1 = -c_t Đ_{12}\Gamma(dx_1/dz);\quad \Gamma = 1 + (x_1/\gamma_1)(\partial\gamma_1/\partial x_1) \tag{7}$$

A comparison of relation (1) with equation (7) shows that the Fick diffusivity equals the M-S diffusivity $Đ_{12}$ times the thermodynamic factor Γ, also referred to as the "Darken correction factor"

$$D_{12} = Đ_{12}\Gamma \tag{8}$$

Darken[20] was one of the first to recognize the need to use activity gradients as proper driving forces when setting up the phenomenological relations to describe diffusion in metal alloys.

In order to appreciate the strong influence of Γ on the Fick diffusivity, let us consider diffusion in methanol(1)/n-hexane(2) mixtures which has an upper critical solution temperature (UCST) of 308 K, and a critical composition x_1 = 0.5. The phase equilibrium diagram is shown in Figure 10a. Figure 10b presents calculations of the Γ as a function of the mole fraction of methanol, x_1, for five different temperatures. At any temperature, T, there is an order of magnitude decrease of Γ as x_1 approaches the critical composition from either end of the composition range. The severe reduction in the magnitude of Γ gets reflected in a corresponding decrease in the magnitude of the Fick diffusivity D_{12}; see

experimental data[21] in Figure 10c. If we "factor out" the influence of Γ, we find that the M-S diffusivity $Đ_{12}$ is "well-behaved" and varies only by a factor of two; see Figure 10d. A plot of the logarithm of $Đ_{12}$ versus the x_1 follows a straight-line dependence to a reasonable approximation; this suggests the interpolation formula $Đ_{12} = \left(Đ_{12}^{x_1 \to 1}\right)^{x_1} \left(Đ_{12}^{x_2 \to 1}\right)^{x_2}$ for estimating the $Đ_{12}$ from the infinite dilution values at either ends of the composition range: $Đ_{12}^{x_1 \to 1}$, and $Đ_{12}^{x_2 \to 1}$.

In the experiments reported by Vitagliano et al.[22], the Fick diffusivities, D_{12}, for triethylamine (1)/water (2) mixtures were measured at 293.15 K, slightly above the value of UCST = 291.5 K, at varying compositions approaching the spinodal curve from either side; see Figure 10e. Their data clearly demonstrate that the diffusivities vanish at spinodal composition.

Diffusion near meta-stable and supersaturation regions is of crucial importance in crystal growth. The diffusivity of urea, and glycine in water plummets to vanishingly low values as the spinodal compositions are reached;[23, 24] see Figure 10f. The strong concentration dependence of $Đ_{12}$ is dictated by the thermodynamic factor Γ. It is common practice to use chemical potential differences between the supersaturated solution (the transferring state) and the crystal (the transferred state), $\left(\mu_i - \mu_{i,eq}\right)/RT = \ln\left(a_i / a_{i,eq}\right)$, as the driving force to model crystal growth kinetics.[25]

Within the spinodal envelope, we have phase instability, characterized by $\Gamma < 0$; this implies $D_{12} < 0$ and signals uphill diffusion. In mixtures of metallic alloys and polymeric solutions, uphill diffusion leads to spinodal decomposition.[1] For visualization of the spinodal decomposition phenomena, web links to video animations are provided in the ESI.

For ternary mixtures, Equation (6) can be shoe-horned into the Fickian form (4), yielding an explicit expression for $[D]$

$$\begin{bmatrix} D_{11} & D_{12} \\ D_{21} & D_{22} \end{bmatrix} = \frac{\begin{bmatrix} Đ_{13}\left(x_1 Đ_{23} + (1-x_1) Đ_{12}\right) & x_1 Đ_{23}\left(Đ_{13} - Đ_{12}\right) \\ x_2 Đ_{13}\left(Đ_{23} - Đ_{12}\right) & Đ_{23}\left(x_2 Đ_{13} + (1-x_2) Đ_{12}\right) \end{bmatrix}}{x_1 Đ_{23} + x_2 Đ_{13} + x_3 Đ_{12}} \begin{bmatrix} \Gamma_{11} & \Gamma_{12} \\ \Gamma_{21} & \Gamma_{22} \end{bmatrix} \qquad (9)$$

The M-S diffusivities of the constituent binary pairs $Đ_{12}$, $Đ_{13}$, and $Đ_{23}$ can be estimated from the infinite dilution values, six in total, using the same interpolation formula as illustrated in Figure 10d;[26] details are provided in the ESI. When these estimations are combined with the calculations of Γ_{ij} from phase equilibrium thermodynamics, Equation (9) affords an estimate of $[D]$. We will see in the ensuing discussions that coupling effects in ternary liquid diffusion emanate to a large extent from contributions of the off-diagonal elements of $[\Gamma]$.

In the homogeneous single phase region, the requirement of phase stability implies $|\Gamma| \geq 0; \quad |D| > 0$. Consequently, the eigenvalues of $[D]$ must each be positive definite.[4] The limits of phase stability defines the spinodal curve, along which we must satisfy $|\Gamma| = 0; \quad |D| = 0$. Within the spinodal envelope, the conditions of phase instability prevail, and $|\Gamma| < 0; \quad |D| < 0$; this implies demixing and splitting into two liquid phases.

Diffusivity measurements in ternary mixtures yield the four elements of [D];[27] the interpretation of the diffusivity data requires us to "factor out" the thermodynamic influences portrayed in $[\Gamma]$. Experimental data on [D] for glycerol/acetone/water mixtures at various compositions in the acetone-rich and water-rich regions are available.[27] For example, at x_1= 0.1, x_2 = 0.432, x_3 = 0.468, we find $[D] = \begin{bmatrix} 0.490 & 0.227 \\ 0.458 & 0.399 \end{bmatrix} \times 10^{-9}$ m^2 s^{-1}. The large magnitudes of the off-diagonal elements signal strong diffusional coupling. The matrix of thermodynamic factors at this composition is calculated from phase equilibrium data, $[\Gamma] = \begin{bmatrix} 1.442 & 0.533 \\ 0.958 & 0.409 \end{bmatrix}$. The large off-diagonal elements of $[\Gamma]$ contribute to the off-diagonal elements of $[D]$, which in turn have the potential to induce uphill transport.

Figure 11a plots the determinant $|D|$ as a function of the mole fraction of glycerol, x_1. Increasing the glycerol composition, decreases ; as the plait point is approached, $|D|$ tends to vanish. Figure 11b shows the variation of the ratios D_{12}/D_{11}, and D_{21}/D_{22} as a function of $|D|$. We note that as $|D|$ is lowered, both

D_{12}/D_{11}, and D_{21}/D_{22} tends to increase. In other words, coupling effects become stronger as the spinodal curve is approached from the homogeneous single-phase region. In order to demonstrate that diffusional coupling effects are primarily caused by thermodynamic coupling effects, Figure 11c compares the ratios D_{12}/D_{11}, and Γ_{12}/Γ_{11} as a function of $|D|$. The observed inter-relation between the two independent data sets is anticipated by equation (9). We conclude that diffusional coupling effects in liquid mixtures are deeply rooted in non-ideal solution thermodynamics.

Similar conclusions are derived by examination of the diffusivity data for water/chloroform/acetic-acid mixtures,[28, 29] measured at different compositions in the homogeneous single-phase region; see Figure 12. At the composition richest in acetic acid, $[D] = \begin{bmatrix} 0.97 & 0.13 \\ 0.073 & 1.259 \end{bmatrix} \times 10^{-9}$; at the composition close to the binodal curve $[D] = \begin{bmatrix} 0.309 & 0.368 \\ 0.344 & 0.939 \end{bmatrix} \times 10^{-9}$. A cursory data examination indicates that the determinant $|D|$ decreases in magnitude as the binodal curve is approached; concomitantly, the off-diagonal elements become larger in magnitude. To quantify this observation, Figure 13a presents a plot of $|D|$ as a function of (1 - x_3). We note that as the mixture becomes poorer in acetic acid, $|D|$ decreases progressively. At the plait point (composition: x_1 = 0.375, x_2 = 0.261 and x_3 = 0.364), we have $[D] = \begin{bmatrix} 0.92 & 0.40 \\ 0.37 & 0.161 \end{bmatrix} \times 10^{-9}$, and $|D| = 0$. The variation of $|\Gamma|$ with (1 - x_3) shows analogous characteristics (cf. Figure 13b) indicating the intertwining of diffusivity and non-ideal solution thermodynamics. The dependence of the ratios D_{12}/D_{11}, and D_{21}/D_{22} on the magnitude of $|D|$ is shown in Figure 13c; coupling effects become stronger as the region of meta-stability is approached.

With the above data and insights, let us determine equilibration trajectories for inter-diffusion of glycerol/acetone/water mixtures of two different compositions, that equilibrate to x_1= 0.1, x_2 = 0.432, x_3 = 0.468. For determination of the equilibration trajectory, we use the experimental value $[D] = \begin{bmatrix} 0.490 & 0.227 \\ 0.458 & 0.399 \end{bmatrix} \times 10^{-9}$ at the final equilibrated composition. In two-dimensional (2D) mole

fraction space, a serpentine trajectory is obtained; see Figure 14a. The observed overshoots and undershoots imply uphill diffusion for glycerol.

What is the contribution of $[\Gamma]$ to the overshoots observed for glycerol? To address this question we calculated the trajectories assuming that the first right member of equation (9) is a scalar diffusivity with the value 1×10^{-9} $m^2\ s^{-1}$, and take $[\Gamma]=\begin{bmatrix}1.442 & 0.533\\ 0.958 & 0.409\end{bmatrix}$ calculated from phase equilibrium data for x_1= 0.1, x_2 = 0.432, x_3 = 0.468. In this scenario, the resulting trajectory is shown by the dashed line in Figure 14a. A similar serpentine trajectory results, leading us to conclude that the uphill diffusion characteristics largely stem from the off-diagonal elements of $[\Gamma]$.

Does glycerol transfer against its activity driving force? To answer this question, we determined the component activities, $a_i = \gamma_i x_i$, at each position on the equilibration trajectory. When the trajectory is plotted in 2D activity space, we observe a monotonous equilibration process (cf. Figure 14b). This is an important result, indicating that glycerol diffusion is not uphill of its activity driving force. To further strengthen this conclusion, Figure 14c compares the glycerol profiles as a function of the distance from the interface. The activity profile of glycerol does not exhibit any overshoots or undershoots.

The findings of Figure 14 can be summarized as follows. Overshoots, and undershoots in *composition space* are largely due to thermodynamic coupling effects. If the diffusion process is viewed in *activity space*, the diffusion characteristics are "normal"; the process of diffusion is downhill of its activity gradient.

Can a serpentine trajectory foray into meta-stable regions? We investigate the equilibration process for the system water(1)/chloroform(2)/acetic-acid(3) in which the two mixtures are allowed to equilibrate to the equilibrium composition: $x_{1,eq}$ = 0.34, $x_{2,eq}$ = 0.24 and $x_{3,eq}$ = 0.42; the diffusivity data at this composition is indicated in Figure 13a. We see that the acetic-acid undershoot has penetrated the binodal envelope into the meta-stable zone; this suggests the possibility of emulsification.[15] Use of Equation (2) will result in straight-line equilibration trajectory (shown as dashed line); in this case, no

emulsification is feasible. If the objective is the produce meta-stable dispersions,[18, 19] a precise prediction of the equilibration trajectory is of vital importance.

Figure 13b presents the equilibration trajectories in water(1)/2-propanol(2)/cyclohexane(3) for the equilibrium composition x_1= 0.36, x_2 = 0.4, x_3 = 0.24, that lies just above the plait point at the critical temperature T_c = 303.67. The equilibration trajectories are calculated at four different temperatures, 303.75 K, 304.15 K, 304.65 K, 396.65 K. At all four temperatures, the equilibration trajectories penetrate the binodal curve. The closer the temperature is to the critical temperature, T_c = 303.67 K, the deeper is the penetration. As a consequence, we should expect phase splitting should ensue in all the four cases; straight-line equilibration trajectories would not anticipate phase splitting in any of the four temperature scenarios.

The ESI provides detailed analyses of the transient equilibration trajectories in seven other partially miscible mixtures: acetone/water/ethylacetate, water/acetone/toluene, toluene/ethanol/water, water/caprolactam/toluene, water/caprolactam/benzene, toluene/propionic-acid/water, and ethylacetate/propionic-acid/water. In all the seven cases, serpentine trajectories are found to enter the meta-stable regions allowing for emulsification.

Based on the foregoing results and observations, we would be tempted to conclude that equilibration trajectories for non-ideal liquid mixtures are never linear. This conclusion would be erroneous in the event that the equilibrated composition lies on the spinodal curve. As proof, let us investigate inter-diffusion in glycerol/acetone/water mixtures of different compositions that equilibrate to a composition that corresponds to the plait point (x_1 = 0.1477, x_2= 0.4163, x_3= 0.4360). The diffusivity value at this composition is $[D]=\begin{bmatrix} 0.42 & 0.35 \\ 0.3 & 0.24 \end{bmatrix}\times 10^{-9}$, and $|D|=0$ because this is the stability limit. Consequently, one of the eigenvalues of [D] must vanish and the equilibration of all components must relax along the eigenvector corresponding to the non-zero eigenvalue $D_{eig,1}=0.67\times 10^{-9}$.[16] In the 2D composition space, the trajectory is linear, at a tangent to the binodal curve; see Figure 16a. The straight-line trajectory is confirmed in experiments.[16] Figure 16b shows a similar straight-line trajectory for

equilibration in water/chloroform/acetic-acid mixtures for conditions such that the equilibrium composition corresponds to the plait point for this system. The results in Figure 16 appear paradoxical because coupling effects are strongest when $|D| \approx 0$, as has been established in Figures 11, and 13.

Looking back, the phenomenon of uphill diffusion that was observed for ideal gas mixtures appears quite extraordinary, because no thermodynamic influences are in play for mixtures of ideal gases.

4. Uphill diffusion in mixtures of metals, alloys, and glasses

The proper prediction of equilibration trajectories in mixtures of metals, glasses, steels, alloys, and composites is important in a wide variety of processes such as bonding, cladding, controlled heat treatments, and surface modification.[1, 7, 20, 30]

One of the very first experimental evidence of uphill diffusion is available in the classic experiments reported by Darken.[20] The following three quotes from his 1949 paper also serve as learning points for this tutorial review

"*the driving force in an isothermal diffusion process may be regarded as the gradient of the chemical potential,*",

"*for a system with more than two components it is no longer necessarily true that a given element tends to diffuse toward a region of lower concentration even within a single phase region*", and

"*departure from the behavior of an ideal solution may be so great that the concentration gradient and the chemical potential gradient, or activity gradient, may be of different sign, thus giving rise to uphill diffusion*".

In one of the Darken experiments, two austenite bars of different compositions (0.48% C, 3.8% Si), and (0.45% C, 0.05% Si) are welded together. The carbon in the high-Si bar has a significantly higher chemical potential or activity than the bar with the lower Si content. After Carbon was allowed to diffuse for 13 days at 1323 K, most of the C diffused into the low-Si bar; see Figure 17a. The overshoot and undershoot in the %C are adequately modelled for the ternary C/Si/Fe mixture with the values of the

Fick diffusivity matrix $[D]=\begin{bmatrix}480 & 34\\ 0 & 2.3\end{bmatrix}\times 10^{-13}$. The high C content near the surface of the austenite bar on the right, imparts the required "hardness". The process of hardening of steel by "carburizing" is reliant on uphill transport of carbon from the high-Si bar to the low-Si bar, despite the fact that the initial compositions of carbon are practically the same in the two adjoining bars.

Consider the equilibration process when glass slabs with two different compositions of $K_2O(1)/SrO(2)/SiO_2(3)$ are brought into contact at time t=0. The wt% of each component is measured on either side interface, measured at t = 4.55 h after the start of the experiment are shown in Figure 17b.[30] The overshoot and undershoot in the SrO concentrations are adequately modelled taking $[D]=\begin{bmatrix}1 & -0.267\\ -1.22 & 0.33\end{bmatrix}\times 10^{-13}$. The uphill transport of SrO is primarily attributable to the large value of D_{21}, that is opposite in sign to D_{22}. Uphill transport in mixtures of glasses can be harnessed to enhance the physical properties.

For inter-diffusion of Fe(1)/Mg(2)/Ca(3) mixtures in garnet,[7] the trajectories indicated by the continuous solid lines in Figure 3 are calculated using $[D]=\begin{bmatrix}5.86 & -1.02\\ -5.5 & 1.18\end{bmatrix}\times 10^{-19}$. The primary reason for uphill transport of Mg is the extremely large value of D_{21}, opposite in sign to D_{22}.

In the three foregoing examples, the large values of off-diagonal elements of $[D]$ are primarily attributable to the off-diagonal elements of matrix $[\Gamma]$. In other words, the equilibration trajectories are monotonous when viewed in activity space.

Uphill diffusion and serpentine equilibration trajectories are routinely encountered in the processing of ceramics, cements, alloys, steels, and composites.[1, 7, 20, 30]

5. Crossing "forbidden" boundaries in azeotropic distillation

Distillation is the most widely used separation process in the chemical process industries. Design procedures for distillation are commonly based on the equilibrium stage model, developed by Sorel more than a hundred years ago.[31] Departures from thermodynamic equilibrium between the vapor and

liquid phases on a distillation tray (see schematic in Figure 18), are commonly accounted for by introducing the Murphree component efficiencies $E_{i,MV} = \left((y_{iL} - y_{iE}) / (y_i^* - y_{iE}) \right)$ where y_{iE}, and y_{iL} are, respectively, the vapor phase mole fractions, entering and leaving a tray, and y_i^* is the vapor composition in thermodynamic equilibrium with the liquid leaving the tray. For a tray in thermodynamic equilibrium, the component efficiencies are 100% for each component. Diffusional transfer resistances on either side of the vapor/liquid interface reduce the component efficiencies to values below 100%. For binary distillation, the Murhpree component efficiencies are bounded, i.e. $0 \le E_{1,MV} = E_{2,MV} \le 1$. For ternary mixtures, coupled diffusion effects in either vapor or liquid phases cause the component efficiencies to be distinctly different from one another, $E_{1,MV} \ne E_{2,MV} \ne E_{3,MV}$. Phenomena such as osmotic diffusion, diffusion barrier, and uphill diffusion result in Murphree component efficiencies that are unbounded ($E_{i,MV} \to \pm\infty$), zero ($E_{i,MV} = 0$), or negative ($E_{i,MV} < 0$); this has been demonstrated in several experimental studies.[4, 32]

Consider distillation of water(1)/ethanol(2)/acetone(3) mixtures. The pure component boiling points are: water = 373.2 K; ethanol = 351.6 K; acetone = 329.7 K; water/ethanol azeotrope = 351.4 K (composition of azeotrope = 12% water, 88% ethanol). Ethanol is the component with the intermediate boiling point. Consequently, the transfer of ethanol is from the liquid to the vapor phase near the top of the distillation column, approaching the condenser. However, ethanol transfers from the vapor to the liquid phase near the bottom of the column approaching the reboiler. This implies that the driving force for transfer of ethanol, $\left(y_2^* - y_{2E} \right)$, must necessarily change sign from the bottom to the top of the column. At some intermediate position, we may also have the situation corresponding to $\left(y_2^* - y_{2E} \right) = 0$. For one set of experiments,[32, 33] the values of $\left(y_2^* - y_E \right)$ are plotted in Figure 19a. We note that the ethanol driving force is negative for Stages 2 – 9, $\left(y_2^* - y_E \right) \approx 0$ for Stage 10, and $\left(y_2^* - y_{2E} \right) > 0$ for Stage 11. The values of the $E_{2,MV}$ for ethanol is negative on Stage 10; on Stage 11, $E_{i,MV} > 1$; see Figure

19b. This implies uphill diffusion on stages 10 and 11; the transfer of ethanol (2) is dictated by the driving forces of the partner species $\left(y_1^* - y_{1E}\right)$, and $\left(y_3^* - y_{3E}\right)$, that are both finite.[32, 33]

Unequal component efficiencies, $E_{1,MV} \neq E_{2,MV} \neq E_{3,MV}$, influence the composition trajectories followed by the vapor and liquid phase along the distillation column. Generally speaking, residue curve maps provide a good indication of the composition trajectories along the distillation column in which all the component efficiencies are equal to one another $E_{1,MV} = E_{2,MV} = E_{3,MV}$.[33] In other words, the residue curve maps chart out the trajectories that must be followed if diffusional limitations are insignificant. Figure 20a shows the residue curve map for water/ethanol/acetone distillation. The thick solid black line is the distillation boundary; this boundary cannot normally be crossed during distillation.[33]

For one set of starting conditions, the experimentally determined composition trajectories (indicated by symbols in Figure 20b), follows a circuitous path, deviating from the residue curve map. Also shown are the trajectories calculated by the Equilibrium (EQ) stage model ($E_{1,MV} = E_{2,MV} = E_{3,MV} = 1$) and the Non-Equillibrium (NEQ) stage model (properly accounting for the diffusional coupling effects in both vapor and liquid phases). The NEQ model correctly traces the experimentally observed circuitous path. The EQ model predicts a trajectory strictly adheres to the trajectory dictated by the residue curve. The circuitous path followed in the experiments is indicative of uphill transport somewhere along the distillation column.

The experimental composition trajectories in Figure 20c for a different set of starting conditions, indicate that the "forbidden" boundary is crossed. The NEQ model is able to retrace this boundary-crossing trajectory, and correctly predicts that the column gets progressively richer in water as we proceed down the column to the reboiler. The EQ model anticipates that the column gets enriched in ethanol, staying on the left side of the boundary. Uphill transport has the effect of changing the *direction* of composition variation in the distillation column.

For heterogeneous azeotropic distillation of water/ethanol/cyclohexane, and water/acetone/toluene (cf. Figure 21), the experimental data also show boundary crossing effects that can be rationalized by accounting for coupled diffusion effects.[34, 35]

The deliberate exploitation of uphill transport to achieve "impossible" distillation separations provides an intriguing and fertile area of research activity.[31]

6. Ionic diffusion and the influence of electrostatic potential gradients

Coupled diffusion effects, including uphill diffusion, are important in ion exchange and electrodialysis separations.[2] The origin of such coupling effects are different to those discussed earlier, and emanate from electrostatic effects. For transport of ionic species in electrolyte solutions, we need to consider the electrostatic potential gradient as an additional driving force for transport. The flux relations for transport of ionic species *i* are obtained by adding $-x_i z_i (\mathrm{F}/RT)(d\Phi/dz)$ to the left member of equation (6), where z_i is the charge on species *i*, and F is the Faraday constant. The *n*th species is usually water (W), that is commonly present in significantly large quantities, and can often be considered stagnant, $N_W = c_W u_W = 0$. For dilute aqueous solutions of electrolytes, the ion-ion interactions can often be neglected, and thermodynamic non-ideality effects are often, but not always, negligible; so $(x_i/RT)(d\mu_i/dz) \approx (dx_i/dz)$. With these modifications and assumptions, equation (6) reduces to the Nernst-Planck equation $N_i = -Đ_{iw}\dfrac{dc_i}{dz} - c_i z_i Đ_{iw}\dfrac{\mathrm{F}}{RT}\dfrac{d\Phi}{dz}$ for the ionic flux with respect to water; here $Đ_{iw}$ is the ion-water diffusivity. If there is no flow of current, we have the electroneutrality constraint $\sum_{i=1}^{n-1} z_i \mathrm{F} N_i = 0$. The maintenance of electroneutrality induces a *diffusion potential* $\dfrac{d\Phi}{dz} = -\left[\left(\sum_{i=1}^{n-1} z_i Đ_{iw}\dfrac{dc_i}{dz}\right)\Big/\left(\dfrac{\mathrm{F}}{RT}\sum_{i=1}^{n-1} c_i z_i^2 Đ_{iw}\right)\right]$. The effective diffusivity of ionic species *i* is $D_{i,eff} \equiv -\left(N_i \Big/ \dfrac{dc_i}{dz}\right) = Đ_{iw} + \left(\left(c_i z_i Đ_{iw}\dfrac{\mathrm{F}}{RT}\dfrac{d\Phi}{dz}\right)\Big/\left(\dfrac{dc_i}{dz}\right)\right)$. The induced diffusion potential has the effect

of influencing the motion of each of the ionic species. The second term on the right serves either to accelerate or decelerate each species, depending on the charges, z_i, and individual ionic mobilities $Đ_{iw}$.

With this theoretical background, let us examine data of Vinograd and McBain[36] for ionic diffusivities determined in a two-compartment diffusion cell.. The top compartment contains an aqueous solution of HCl and $BaCl_2$; the bottom compartment contains pure water; see Figure 22a. Diffusion takes place through the pores of a sintered glass disk that separates the two compartments. On complete ionization, the mixture consists of the ionic species H^+, Cl^-, Ba^{2+} and un-ionized H_2O. By monitoring the concentrations of the three ionic species as a function of time, the effective ionic diffusivities D_i for H^+, Cl^- and Ba^{2+} are determined. The ionic diffusivities are plotted in Figure 22a as function of the square root of the ratio of the initial ionic concentrations of H^+ and Ba^{2+} in the top compartment $\sqrt{c_{H+}/c_{Ba2+}}$. With increasing values of $\sqrt{c_{H+}/c_{Ba2+}}$, it is observed that both D_{H+} and D_{Ba2+} decrease while D_{Cl-} increases.

During the start of the diffusion process, the highly mobile H^+ diffuses ahead of its companion ions, creating an excess of positive charge in the bottom compartment. This induces a potential $d\Phi/dz$, which acts in such a way as to maintain electro-neutrality. As a consequence, Cl^- experiences an extra "pull", enhancing its effective diffusivity value. The contribution of $d\Phi/dz$ also serves to retard the motion of the cations H^+ and Ba^{2+}; in other words, the cations experience a "push" in a direction opposite to that dictated by their composition gradient driving forces. For $\sqrt{c_{H+}/c_{Ba2+}} = 2$, the electrostatic "push" on Ba^{2+} results in a vanishing value for D_{Ba2+}. The continuous solid lines in Figure 22a are the calculations of the effective diffusivities using the Nernst-Planck equation. For $\sqrt{c_{H+}/c_{Ba2+}} > 2$, negative values of D_{Ba2+} are obtained, signifying that uphill diffusion of Ba^{2+} is feasible.

The sign of the engendered diffusion potential $d\Phi/dz$ is dictated by the concentration gradients of the individual ions and is therefore dependent on the signs (i.e. directions) of the concentration gradients. This directional influence of the diffusion potential is illustrated clearly by the experiments for external

mass transfer limited ion exchange; see Figure 22b. Exchanging Na^+ within the ion exchange bead with H+ from the bulk chloride solution proceeds at a significantly higher rate than for the reverse exchange process.[2]

Figure 23 presents experimental data for transient transport of H^+, Na^+, and Cs^+ ions across a Nafion cation exchange membrane, separating acid and salt compartments.[37] The HSO_4^- and SO_4^{2-} ions cannot cross the membrane. The H^+ ions transfer from the acid to the salt compartment. Both Na^+, and Cs^+ ions transfer from the salt to the acid compartment. Due to the significantly higher mobility of the H^+ ions, an excess positive charge is created in the salt compartment. This induces a potential $d\Phi/dz$ that tends to accelerate the motion of the Na^+, and Cs^+ ions out of the salt compartment into the acid compartment. Since the concentration driving force of Cs^+ ions is very small, the initial transience is dominated by the contribution of $d\Phi/dz$; this results in the observed overshoot in the equilibration of Cs^+.

Uphill diffusion can be exploited to recover trace quantities of valuable components from aqueous solutions.

7. Reverse osmosis

The best known example of uphill diffusion is in the reverse osmosis (RO) process for desalination, in which fresh water is recovered from saline water by use of a polyamide film membrane that rejects salt, and allows only water to permeate; see Figure 24.[2]

In reverse osmosis, the driving force for transport across the polyamide membrane layer must additionally account for the contribution of the pressure gradients. The water flux across the membrane is described by adding the contribution of the pressure gradient to the left member of equation (6): $-\frac{x_w}{RT}\frac{d\mu_w}{dz}-\frac{1}{RT}\overline{V}_w\frac{dp}{dz}=\frac{N_w}{c_t Đ_{wM}}$, where $\overline{V_w}$ is the partial molar volume and $Đ_{wM}$ is the diffusivity of water through the membrane; we ignore diffusional interactions between water and salt. For a membrane of thickness δ, we obtain $-\frac{\Delta x_w}{\delta}-\frac{1}{RT}\overline{V}_w\frac{\Delta p}{\delta}=\frac{N_w}{c_t Đ_{wM}}$ for dilute salt solutions for which thermodynamic non-idealities are negligible. In desalination operations, the upstream compartment will typically have 2

mole % salt and the downstream compartment will be practically salt-free. Therefore, the driving force for water transport $\Delta x_w = 1.0 - 0.98 = 0.02$. If no additional pressure is applied to the upstream compartment, the pressure difference at equilibrium, corresponding to $N_w = 0$, is called the osmotic pressure $\Delta p = \Pi = -\frac{RT\Delta x_w}{\overline{V}_w}$. Typically, $T = 298$ K, and $\overline{V_w} = 1.8 \times 10^{-5}$ m^3 mol^{-1}; the osmotic pressure is 2.75 MPa. In order to drive water from the left to right across the membrane, we need to apply Δp values exceeding 2.75 MPa. Water is pumped uphill by application of a Δp across the membrane.

In electro-osmosis, water is dragged uphill by electrostatic potential gradients.[2]

8. Diffusion in microporous crystalline materials

Ordered crystalline microporous materials such as zeolites (crystalline aluminosilicates), and metal-organic frameworks (MOFs) have applications in processes such as CO_2 capture, H_2 production, natural gas purification, hydrocarbons separations, and air separations.[3, 38, 39] The technologies used in industrial separations are either pressure swing adsorption (PSA) units[3] or membrane permeation devices.[2, 40, 41] The operations of fixed bed adsorption units are intrinsically transient in nature, i.e. the gas (or fluid) phase concentrations vary both with time, and distance along the adsorber.

The separation of N_2/CH_4 mixtures is important in the context of natural gas upgrading. For transportation purposes, the pipeline specifications usually demand that the amount of N_2 in natural gas is less than about 3%, because the presence of N_2 reduces the heating value. For purification of natural gas streams, it is desirable to use adsorbents in PSA units that are selective to N_2. For most known adsorbents, the adsorption selectivity favors CH_4. One practical solution to this separation problem is to rely on diffusion selectivities by use of microporous LTA-4A zeolite, that consists of cages of about 11 Å size, that are connected by 4 Å window apertures. Nitrogen is a "pencil-like" molecule (4.4 Å × 3.3 Å; see Figure 25a) that can hop length-wise across the narrow windows; the "spherical" CH_4 (3.7 Å) is much more severely constrained and has a diffusivity that is 22 times lower than that of N_2. Video

animations, obtained from MD simulations, showing the hopping of N_2, and CH_4 molecules across the 4 Å windows are available as ESI.

The earliest study demonstrating the possibility of exploiting diffusion selectivities for separating N_2/CH_4 mixtures is due to Habgood,[42] who presents experimental data on transient mixture uptake within LTA-4A (cf. Figure 25b). During the initial stages of the transient uptake, the pores of LTA-4A are predominantly richer in the more mobile N_2, but this is displaced by the more strongly-adsorbed-but-tardier CH_4 molecules at longer times. This results in an overshoot in the N_2 loading within the crystals during the early stages of transience. Note that the maximum loading of N_2 is about a factor 2.5 times that of the final equilibrated uptake. Put another way, supra-equilibrium loadings are attained for N_2 during a short time interval; we infer the occurrence of uphill diffusion. Based on his experimental results, Habgood filed a patent claiming that natural gas could be upgraded by selectively adsorbing the faster diffusing nitrogen in a diffusion-selective PSA process employing LTA-4A zeolite.

Let us model the intra-crystalline diffusion of N_2 and CH_4 within the pores of LTA-4A. The M-S Equation (6) for bulk fluid mixtures is a good starting point for setting up the flux expressions, but needs to be adapted and extended. Each of the constituent species hops across the windows one-at-a-time; the inter-cage hopping of each species occurs independent of its partner. Therefore, the term portraying *i-j* pair interactions can be ignored, as a reasonable approximation. Let $Đ_1$ and $Đ_2$ reflect the diffusivities for inter-cage hopping; these diffusivities reflect the interactions of guest molecules with the framework walls; we tacitly assume the framework wall to be a pseudo $(n+1)^{th}$ component in the mixture. Within micropores, we are concerned with the motion of adsorbed species; we therefore prefer to use molar loadings of adsorbates, q_i, as concentration measures. The fluxes N_i, defined with respect to the fixed framework wall, are written in the following form[43-45]

$$-\rho\frac{q_1}{RT}\frac{d\mu_1}{dz}=\frac{N_1}{Đ_1};\quad -\rho\frac{q_2}{RT}\frac{d\mu_2}{dz}=\frac{N_2}{Đ_2} \tag{10}$$

where ρ is the framework density. The chemical potential gradients $d\mu_i/dz$ can be related to the gradients of the molar loadings, q_i, by defining thermodynamic correction factors Γ_{ij}

$$\frac{q_i}{RT}\frac{d\mu_i}{dz} = q_i \frac{d\ln p_i}{dz} = \sum_{j=1}^{n} \Gamma_{ij} \frac{dq_j}{dz}; \quad \Gamma_{ij} = \frac{q_i}{p_i}\frac{\partial p_i}{\partial q_j}; \quad i, j = 1,....n \tag{11}$$

Combining equations (10) and (11) we obtain for binary mixtures

$$\begin{pmatrix} N_1 \\ N_2 \end{pmatrix} = -\rho \begin{bmatrix} Đ_1 & 0 \\ 0 & Đ_2 \end{bmatrix} \begin{bmatrix} \Gamma_{11} & \Gamma_{12} \\ \Gamma_{21} & \Gamma_{22} \end{bmatrix} \begin{pmatrix} \frac{dq_1}{dz} \\ \frac{dq_2}{dz} \end{pmatrix} \tag{12}$$

Coupled diffusion effects have their origins in mixture adsorption thermodynamics. The elements Γ_{ij} can be determined from models such as the mixed-gas Langmuir model or the Ideal Adsorbed Solution Theory (IAST) for describing mixture adsorption equilibrium; these models allow calculation of the component molar loadings q_1 and q_2, on the basis of partial pressures p_1 and p_2 in the bulk gas phase surrounding the microporous crystals.

The calculations of the elements of the matrix of thermodynamic factors Γ_{ij} for N_2/CH_4 mixture in LTA-4A crystals demonstrate the significance of the off-diagonal elements at higher loadings; see Figures 25c. We note that for total mixture loadings, $q_t = q_1 + q_2$ less than 0.5 mol kg^{-1}, the off-diagonal elements of the matrix $\begin{bmatrix} \Gamma_{11} & \Gamma_{12} \\ \Gamma_{21} & \Gamma_{21} \end{bmatrix}$ are less than about 0.1. However, for q_t > 1.5 mol kg^{-1}, the off-diagonal elements approach values close to that of the diagonal elements. In other words, thermodynamic coupling effects become increasingly important as the loadings increase.

The continuous solid lines in Figures 25b are solutions to the continuity equations using the flux equation (12); this model successfully captures the overshoot in the uptake of the more mobile N_2. The transient development of component loadings along the radius of the LTA-4A crystal can be visualized in a video animation uploaded as ESI; this animation highlights the occurrence of both temporal and spatial overshoots of N_2 loading within the crystal. The dashed lines in Figure 25b are the simulations in

which thermodynamic factors are ignored and we assume that $\Gamma_{ij} = \delta_{ij}$. Neglect of thermodynamic coupling results in uptake profiles that do not exhibit any overshoot in N_2 uptake. We conclude that off-diagonal contributions of Γ_{ij} cause the N_2 overshoot.

Figure 25d presents calculations of the thermodynamically "corrected" loadings $q_1\mu_1/RT = \Gamma_{11}q_1 + \Gamma_{12}q_2$, and $q_2\mu_2/RT = \Gamma_{21}q_1 + \Gamma_{22}q_2$ as a function of time. It is observed that the equilibration of N_2, measured in terms of the corrected loadings, does not exhibit any overshoot and approaches equilibrium in a monotonic manner. We conclude, therefore, that overshoots have their origin in thermodynamic influences.

For separation of O_2 /N_2 mixtures using carbon molecular sieve (CMS), the adsorption selectivity is in favor of N_2 due to its larger permanent quadrupole compared to that of O_2. However, the diffusivity of N_2 is significantly lower than that of O_2 because of its larger cross-sectional dimension of 3.3 Å, compared to 3.1 Å for O_2. The experimental data for transient uptake of O_2/N_2 mixture in CMS shows an overshoot for the more mobile O_2 (cf. Figure 26). The O_2 overshoot is properly captured by equation (12) with the ratio of diffusivities $Đ_{O2}/Đ_{N2}$ = 37. A video animation showing the transient development of component loadings of N_2 and O_2 along the radius of a CMS particle is available as ESI; this animation demonstrates temporal and spatial overshoots. Carbon molecular sieves can be utilized in a diffusion-selective process for producing purified N_2 gas by selectively adsorbing O_2 during early stages of the transient process.

The essential features of the transient uptake on nC6/2MP uptake in MFI zeolite introduced in Figure 4, can be adequately captured by the flux equation (12) taking $Đ_{nC6}/Đ_{2MP}$ = 100.[8] The lower diffusivity of the mono-branched isomer 2MP is due to the severe configurational constraints within 5.5 Å sized channels of MFI. The nC6 overshoot is caused by the off-diagonal elements of $[\Gamma]$. Video animations showing the transient development of the component loadings along the radius of an MFI crystal are available as ESI; this animation demonstrates the occurrence of both spatial and temporal overshoots for nC6. If we take $\Gamma_{ij} = \delta_{ij}$, the nC6 overshoot disappears.[8] The overshoot of nC6 signifies uphill diffusion

within the crystals during early stages of transience; this phenomenon is advantageous in the PSA process for separation of hexane isomers, deployed in a process for octane enhancement of gasoline.[38]

There is one additional feature of nC6/2MP mixture uptake that distinguishes it from the N_2/CH_4/LTA-4A and O_2/N_2/CMS uptakes. For nC6/2MP/MFI both diffusion and adsorption favor the linear isomer; the two phenomena act in concert to enhance separations.[38]

Mixture diffusion inside micropores has an unique characteristic that makes it different from diffusion in fluid mixtures. For diffusion in bulk fluid mixtures, the two halves of a serpentine trajectory are symmetrical, with an overshoot in one region and a corresponding undershoot in the adjoining region. By contrast, for mixture uptake in microporous materials, there is asymmetry between adsorption and desorption cycles. During the adsorption cycle, the off-diagonal elements become of increasing importance because the total loading increases with time (cf. Figures 25c), whereas in the desorption cycle, influences of coupling decrease because the total loadings decrease with time. For benzene/*p*-xylene mixtures, Niessen and Karge[46] found the adsorption cycle in MFI zeolite proceeds nine times faster than the desorption cycle. The asymmetrical influences of $[\Gamma]$ also cause the adsorption and desorption cycles to follow distinctly different equilibration composition trajectories, as is evident in the results offered in Figure 27 for the three systems (a) N_2/CH_4/LTA-4A, (b) O_2/N_2/CMS, and (c) nC6/2MP/MFI. In all three cases, the desorption cycle does not display any undershoots. The assumption $\Gamma_{ij} = \delta_{ij}$ results in symmetry in the adsorption and desorption trajectories (dashed lines in Figure 27c). Video animations of demonstrating the asymmetry in the transient development of component loadings of N_2, and CH_4 within LTA-4A crystal during both the adsorption and desorption phases are provided as ESI.

Thin layers of microporous materials, of about 50 μm thickness, are used in membrane separation devices.[40, 41] Figure 28a shows the transient permeation of CH_4/nC_4H_{10} mixture across an MFI zeolite membrane.[47] The permeation fluxes are influenced by a combination of adsorption strengths and mobilities. The smaller molecule CH_4 has a mobility about 100 times higher than that of the bulkier *n*-butane. However, CH_4 has a considerably lower adsorption strength. During transient permeation, the

flux of the more mobile CH_4 exhibits a pronounced overshoot during the early stages; the overshoot is adequately captured using the flux equation (12); it is possible to recover CH_4 during early stages of the transience. At the stationary-state, the exit gas is predominantly *n*-butane.

For permeation of xylene isomers across an MFI membrane, the most mobile p-xylene displays an overshoot during early stages of the transience (cf. Figure 28b);[48] this overshoot is dictated by the characteristics of Γ_{ij}.[38]

9. Conclusions

The important messages emerging from this tutorial review are listed below.

(1) Coupling effects in mixture diffusion are often significant, and may cause uphill transport of a species against its concentration gradient. For modelling purposes, the most convenient and practical approach is provided by the Maxwell-Stefan Equation (6). This equation needs to be either extended, or modified, for application to ionic systems, reverse osmosis, and microporous solids. In most cases, the coupling effects have their origins in phase equilibrium thermodynamics.

(2) Transient overshoots, and serpentine equilibration trajectories in composition space are fingerprints of uphill diffusion.

(3) Uphill diffusion may be exploited to separate azeotropes by partial condensation in the presence of an inert non-condensible gas. Coupled diffusion effects often result in the crossing of distillation boundaries for azeotropic distillation that are normally considered “forbidden” when using simpler diffusion models.

(4) Diffusion in the vicinity of phase transition region for mixtures of liquids, metals, alloys, glasses and cements is strongly influenced by the constraints imposed by thermodynamic phase stability. The influence of diffusion coupling becomes increasingly significant as the phase transition region is approached. Serpentine diffusion trajectories may enter meta-stable zones, leading to spontaneous emulsification and the Ouzo effect.

(5) For diffusion in electrolyte solutions, the electrostatic potential gradient, engendered by electroneutrality constants, acts as a leash serving to either accelerate or decelerate the motion of individual ions.

(6) For transient uptake of mixtures within a microporous material, overshoots in loading of the more mobile partner species may occur; these are traceable to the influence of the influence of mixture adsorption thermodynamics. Transient overshoot phenomena may be exploited in diffusion-selective separations. Furthermore, adsorption and desorption processes are not symmetric; they may follow different trajectories.

10. Notation

a_i	activity of species *i*, dimensionless
c_i	molar concentration of species *i*, mol m^{-3}
c_t	total molar concentration of mixture, mol m^{-3}
$Đ_i$	Maxwell-Stefan diffusivity for guest-framework interaction in pore, m^2 s^{-1}
$Đ_{ij}$	M-S diffusivity for *i-j* pair, m^2 s^{-1}
$Đ_{12}$	M-S diffusivity for binary pair 1-2, m^2 s^{-1}
D_{12}	Fick diffusivity for binary pair 1-2, m^2 s^{-1}
$[D]$	Fick diffusivity matrix, m^2 s^{-1}
$\lvert D \rvert$	Determinant of the Fick diffusivity matrix, m^4 s^{-2}
F	Faraday constant, 9.65×10^4 C mol^{-1}
J_i	molar diffusion flux of species *i*, mol m^{-2} s^{-1}
n	number of species in the mixture, dimensionless
N_i	molar flux of species *i* with respect to the pore wall, mol m^{-2} s^{-1}
p_i	partial pressure of species *i* in mixture, Pa
p_t	total system pressure, Pa
q_i	component molar loading of species *i*, mol kg^{-1}
q_t	total molar loading in mixture, mol kg^{-1}
R	gas constant, 8.314 J mol^{-1} K^{-1}
t	time, s
T	absolute temperature, K
x_i	mole fraction, dimensionless
y_i	mole fraction of component *i* in bulk vapor phase, dimensionless
$\overline{V}_i$	partial molar volume of species *i,* m^3 mol^{-1}
z	direction coordinate, m
z_i	charge on species *i*, dimensionless

Greek letters

δ	length of diffusion path or thickness of membrane, m
δ_{ij}	Kronecker delta, dimensionless
γ_i	activity coefficient, dimensionless
$[\Gamma]$	matrix of thermodynamic factors, dimensionless
$\lvert\Gamma\rvert$	Determinant of $[\Gamma]$, dimensionless
μ_i	molar chemical potential, J mol^{-1}
Π	osmotic pressure, Pa
ρ	framework density, kg m^{-3}
Φ	electrostatic potential, V

11. References

1. M. E. Glicksman, *Diffusion in Solids: Field Theory, Solid-state Principles, and Applications*, John Wiley, New York, 2000.
2. J. A. Wesselingh and R. Krishna, *Mass transfer in multicomponent mixtures*, Delft University Press, Delft, 2000.
3. D. M. Ruthven, S. Farooq and K. S. Knaebel, *Pressure swing adsorption*, VCH Publishers, New York, 1994.
4. R. Taylor and R. Krishna, *Multicomponent mass transfer*, John Wiley, New York, 1993.
5. J. B. Duncan and H. L. Toor, *A.I.Ch.E.J.*, 1962, **8**, 38-41.
6. A. J. Reuvers and C. A. Smolders, *J. Membr. Sci.*, 1987, **34**, 67-86.
7. D. Vielzeuf and A. Saúl, *Contrib. Mineral. Petrol.*, 2011, **161**, 683-702.
8. T. Titze, C. Chmelik, J. Kärger, J. M. van Baten and R. Krishna, *J. Phys. Chem. C*, 2014, **118**, 2660-2665.
9. R. Krishna and J. A. Wesselingh, *Chem. Eng. Sci.*, 1997, **52**, 861-911.
10. K. R. Arnold and H. L. Toor, *A.I.Ch.E.J.*, 1967, **13**, 909-914.
11. M. Bres and C. Hatzfeld, *Pflügers Arch.*, 1977, **371**, 227-233.
12. L. Boudin, D. Götz and B. Grec, ESAIM: Proceedings, 2010.http://dx.doi.org/10.1051/proc/2010008
13. J.-C. Chevrolet, *Critical Care*, 2001, **5**, 179–181.
14. D. Fullarton and E. U. Schlünder, *Chem. Eng. Process.*, 1986, **20**, 255-263.
15. K. J. Ruschak and C. A. Miller, *Ind. Eng. Chem., Fundam.*, 1972, **11**, 534-540.
16. R. Krishna, C. Y. Low, D. M. T. Newsham, C. G. Olivera-Fuentes and G. L. Standart, *Chem. Eng. Sci.*, 1985, **40**, 893-903.
17. N. L. Sitnikova, R. Sprik, G. Wegdam and E. Eiser, *Langmuir*, 2005, **21**, 7083-7089.
18. S. A. Vitale and J. L. Katz, *Langmuir*, 2003, **19**, 4105-4110.
19. F. Ganachaud and J. L. Katz, *ChemPhysChem*, 2005, **6**, 209-216.
20. L. S. Darken, *Trans. AIME*, 1949, **180**, 430-438.
21. W. M. Clark and R. L. Rowley, *A.I.Ch.E.J.*, 1986, **32**, 1125-1131.
22. V. Vitagliano, R. Sartorio, E. Chiaravalle and O. Ortona, *J. Chem. Eng. Data*, 1980, **25**, 121-124.
23. A. S. Myerson and D. Senol, *A.I.Ch.E.J.*, 1984, **30**, 1004-1006.
24. Y. C. Chang and A. S. Myerson, *A.I.Ch.E.J.*, 1986, **32**, 1567-1569.
25. M. Louhi-Kultanen, J. Kallas, J. Partanen, Z. Sha, P. Oinas and S. Palosaari, *Chem. Eng. Sci.*, 2001, **56**, 3505-3515.
26. R. Krishna and J. M. van Baten, *Ind. Eng. Chem. Res.*, 2005, **44**, 6939-6947.
27. T. Grossmann and J. Winkelmann, *J. Chem. Eng. Data*, 2007, **52**, 336-340.
28. V. Vitagliano, R. Sartorio, S. Scala and D. Spaduzzi, *J. Solution Chem.*, 1978, **7**, 605-621.
29. D. Buzatu, F. D. Buzatu, L. Paduano and R. Sartorio, *J. Solution Chem.*, 2007, **36**, 1373-1384.
30. A. K. Varshneya and A. R. Cooper, *J. Am. Ceram.. Soc.*, 1972, **55**, 312-317.
31. R. Taylor, R. Krishna and H. Kooijman, *Chem. Eng. Prog.*, 2003, **99 (7)**, 28-39.
32. P. A. M. Springer, R. Baur and R. Krishna, *Sep. Purif. Technol.*, 2002, **29**, 1-13.
33. P. A. M. Springer, B. Buttinger, R. Baur and R. Krishna, *Ind. Eng. Chem. Res.*, 2002, **41**, 1621-1631.
34. P. A. M. Springer, R. Baur and R. Krishna, *Chem. Eng. Res. Des.*, 2003, **81**, 413-426.

35. A. Higler, R. Chande, R. Taylor, R. Baur and R. Krishna, *Comput. Chem. Eng.*, 2004, **28**, 2021-2036.
36. J. R. Vinograd and J. W. McBain, *J. Am. Chem. Soc.*, 1941, **63**, 2008-2015.
37. Y. Yang and P. N. Pintauro, *A.I.Ch.E.J.*, 2000, **46**, 1177-1190.
38. R. Krishna, *Microporous Mesoporous Mater.*, 2014, **185**, 30-50.
39. R. Krishna, *Phys. Chem. Chem. Phys.*, 2015, **17**, 39-59.
40. R. Krishna and J. M. van Baten, *J. Membr. Sci.*, 2013, **430**, 113-128.
41. R. Krishna and J. M. van Baten, *J. Membr. Sci.*, 2011, **383**, 289-300.
42. H. W. Habgood, *Canad. J. Chem.*, 1958, **36**, 1384-1397.
43. R. Krishna, *J. Phys. Chem. C*, 2009, **113**, 19756-19781.
44. R. Krishna, *Chem. Soc. Rev.*, 2012, **41**, 3099-3118.
45. R. Krishna and J. M. van Baten, *Phys. Chem. Chem. Phys.*, 2013, **15**, 7994-8016.
46. W. Niessen and H. G. Karge, *Microporous Mater.*, 1993, **1**, 1-8.
47. E. R. Geus, H. van Bekkum, W. J. W. Bakker and J. A. Moulijn, *Microporous Mater.*, 1993, **1**, 131-147.
48. T. Matsufuji, N. Nishiyama, M. Matsukata and K. Ueyama, *J. Membr. Sci.*, 2000, **178**, 25-34.
49. W. M. Clark and R. L. Rowley, *Int. J. Thermophys.*, 1986, **6**, 631-642.
50. Y. D. Chen, R. T. Yang and P. Uawithya, *A.I.Ch.E.J.*, 1994, **40**, 577-585.

12. Caption for Figures

Figure 1. (a) Flux vs driving force relationship using Fick's law with constant diffusivity. (b) Initial compositions in Bulb A and Bulb B in the two-bulb diffusion experiment. (c) Transient approach to equilibrium in the two-bulb diffusion experiments with $H_2/N_2/CO_2$ mixtures.[5] (d) Equilibration trajectories in composition space.

Figure 2. The immersion precipitation process for membrane preparation.[6] A 10% solution of cellulose acetate (CA) in acetone is immersed in a bath of pure water. The transient equilibration trajectories at three different times, t =10 s, t = 25 s, and t = 50 s are depicted.

Figure 3. (a) Inter-diffusion in a "couple" consisting of Fe/Mg/Ca mixtures.[7] The atom % of each component on either side of the Matano plane (z = 0), measured at t = 100 h after the start of the experiment are shown as function of the distance. (b) Equilibration trajectories in composition space.

Figure 4. Transient uptake of nC6/2MP mixtures in MFI zeolite.[8]

Figure 5. Plot of the normalized flux of nitrogen in $H_2/N_2/CO_2$ gas mixtures plotted as a function of the differences between the compositions in bulbs B and A.

Figure 6. (a) The Loschmidt tube experiment of Arnold and Toor[10] on the transient approach to equilibrium for CH_4(1)/Ar(2)/H_2(3) gas mixtures. (b) Equilibration trajectories in composition space.

Figure 7. Transient equilibration of O_2 in O_2/N_2/He between heliox supply cylinder and patient.

Figure 8. Condensation of an azeotropic mixture of 2-propanol/water in the presence of an inert gas nitrogen results in a condensate which is richer in water than the azeotrope.

Figure 9. Experimental data, measured in a stirred Lewis cell, for the equilibration trajectories followed in the acetone-rich and glycerol-rich phases in the system glycerol/acetone/water.[16]

Figure 10. (a) Liquid/liquid phase equilibrium diagram, (b) Thermodynamic correction factor Γ, (c, d) Fick and M-S diffusivities for methanol(1)/*n*-hexane (2) mixtures.[21] (e) Experimental data of Vitagliano et al.[22] for Fick diffusivities for triethyamine(1)/water(2) mixtures, measured at 293.15 K, for various compositions on either side of the spinodal curve. (f) Fick diffusivitivies of urea, and glycine as a function of solute concentration in aqueous solution.[23, 24]

Figure 11. (a) Determinant of the Fick diffusivity matrix, $|D|$, for glycerol/acetone/water mixtures, as a function of the mole fraction of glycerol, x_1.[27] (b) The ratios D_{12}/D_{11}, and D_{21}/D_{22} as a function of $|D|$. (c) The ratios D_{12}/D_{11}, and Γ_{12}/Γ_{11} plotted as function of $|D|$.

Figure 12. The phase equilibrium diagram for water/chloroform/acetic-acid mixtures at 298 K. The measured values[28, 29] of [D], (units of 10^{-9} m^2 s^{-1}) and determinant $|D|$ (units of 10^{-18} m^4 s^{-2}) are indicated for selected compositions.

Figure 13. (a, b) Plots of the determinants $|D|$ and $|\Gamma|$ as a function of (1- x_3) for water/chloroform/acetic-acid mixtures. (c) The ratios D_{12}/D_{11}, and D_{21}/D_{22} plotted as a function of $|D|$.

Figure 14. (a) Equilibration trajectories in 2D composition space for glycerol/acetone/water mixtures. The equilibrated composition is x_1= 0.1, x_2 = 0.432, x_3 = 0.468. (b) Equilibration trajectories in activity space. (c) Profiles of composition and activity of glycerol as a function of dimensionless distance from the interface.

Figure 15. (a) Equilibration trajectory for inter-diffusion in water/chloroform/acetic-acid mixtures with the equilibrium composition $x_{1,eq}$ = 0.34, $x_{2,eq}$ = 0.24 and $x_{3,eq}$ = 0.42. (b) Equilibration trajectories in water(1)/2-propanol(2)/cyclohexane(3) for the equilibrium composition; the diffusivity values used in these simulations correspond to the experimental data of Clark and Rowley.[49]

Figure 16. Equilibration trajectories for inter-diffusion in (a) glycerol(1)/acetone(2)/water(3), and (b) water(1)/chloroform(2)/acetic-acid(3) mixtures with equilibrium compositions corresponding to the respective plait points: (a) $x_1 = 0.1477$, $x_2 = 0.4163$, $x_3 = 0.4360$, and (b) $x_1 = 0.375$, $x_2 = 0.261$, $x_3 = 0.364$.

Figure 17. (a) Inter-diffusion between austenite bars consisting of C/Si/Fe mixtures.[20] (b) Inter-diffusion between two slabs of $K_2O/SrO/SiO_2$ mixtures.[30]

Figure 18. Schematic of vapor/liquid contacting on a distillation tray.

Figure 19. (a) Ethanol driving force $\left(y_2^* - y_E\right)$ on each stage for the system water(1)/ethanol(2)/acetone(3). (b) Murphree component efficiencies along the column.[32, 33]

Figure 20. (a) Residue curve map for the water(1)/ethanol(2)/acetone(3) system, showing a straight-line distillation boundary and a binary minimum-boiling azeotrope between water and ethanol. (b, c) Experimental data[33] on column composition trajectories for the water/ethanol/acetone system in distillation column operating at total reflux implying $x_i = y_i$. Also shown in (b, c) are the simulation results of the trajectories calculated by EQ and NEQ models.

Figure 21. Experimental data on composition trajectories for distillation of water/acetone/toluene mixtures.[34] The grey shaded area represents the region in which liquid–liquid phase splitting occurs.

Figure 22. (a) Effective ionic diffusivities of H^+, Ba^{++}, and Cl^- in a two-compartment diffusion cell.[36] (b) Transfer rates to and from ion-exchange particles are direction dependent.[2]

Figure 23. Transient concentrations of H^+, Na^+, and Cs^+ in the salt and acid compartments that are separated by a Nafion cation exchange membrane.[37]

Figure 24. Water transport across polyamide-based Reverse Osmosis membrane.[2]

Figure 25. (a) Molecular dimensions of N_2 and CH_4. (b) Transient uptake of N_2/CH_4 mixture in LTA-4A.[42] The solid lines are simulations using (12); the dashed lines are simulations with $\Gamma_{ij} = \delta_{ij}$. (c) Elements of the matrix of thermodynamic factors Γ_{ij} as function of the total mixture loading. (d) Calculations of $\Gamma_{11}q_1 + \Gamma_{12}q_2$, and $\Gamma_{21}q_1 + \Gamma_{22}q_2$ as a function of $t^{1/2}$.

Figure 26. Molecular dimensions of N_2 and O_2, along with transient uptake of O_2/N_2 mixture in CMS.[50]

Figure 27. Comparison of the composition trajectories for the adsorption and desorption cycles for transient adsorption/desorption of (a) N_2/CH_4/LTA-4A, (b) O_2/N_2/CMS, and (c) nC6/2MP/MFI.

Figure 28. Transient permeation of (a) 50/50 CH_4/n-C_4H_{10},[47] and (b) 24/51/25 *p*-xylene/*m*-xylene/*o*-xylene[48] mixtures across MFI membrane.

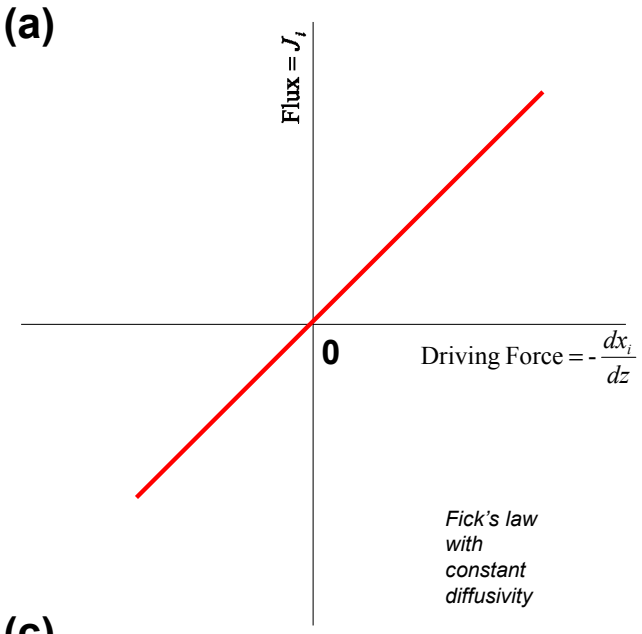
(a)
Flux = J_i
0
Driving Force = $-\frac{dx_i}{dz}$
Fick's law with constant diffusivity

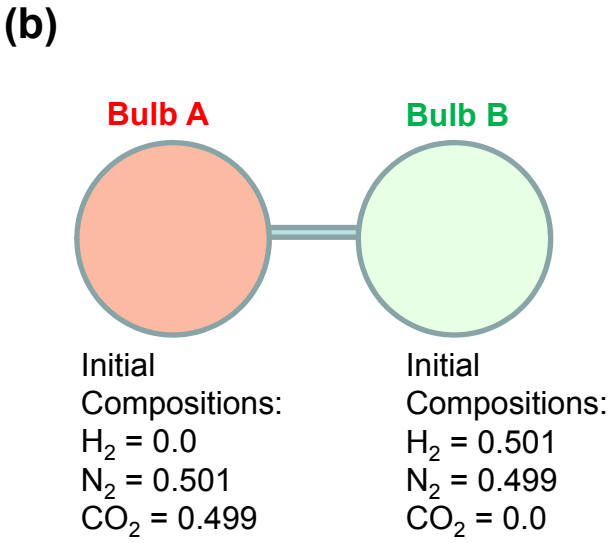
(b)
Bulb A
Bulb B
Initial Compositions:
H_2 = 0.0
N_2 = 0.501
CO_2 = 0.499
Initial Compositions:
H_2 = 0.501
N_2 = 0.499
CO_2 = 0.0

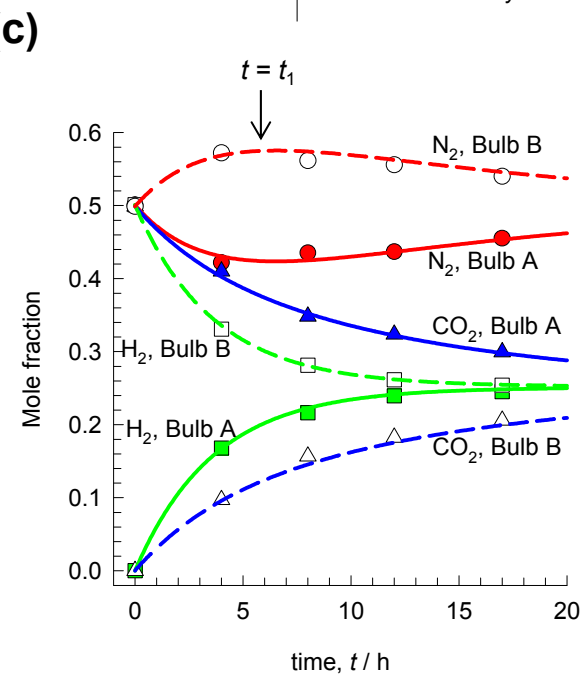
(c)
$t = t_1$
N_2, Bulb B
N_2, Bulb A
CO_2, Bulb A
H_2, Bulb B
H_2, Bulb A
CO_2, Bulb B
Mole fraction
time, t / h

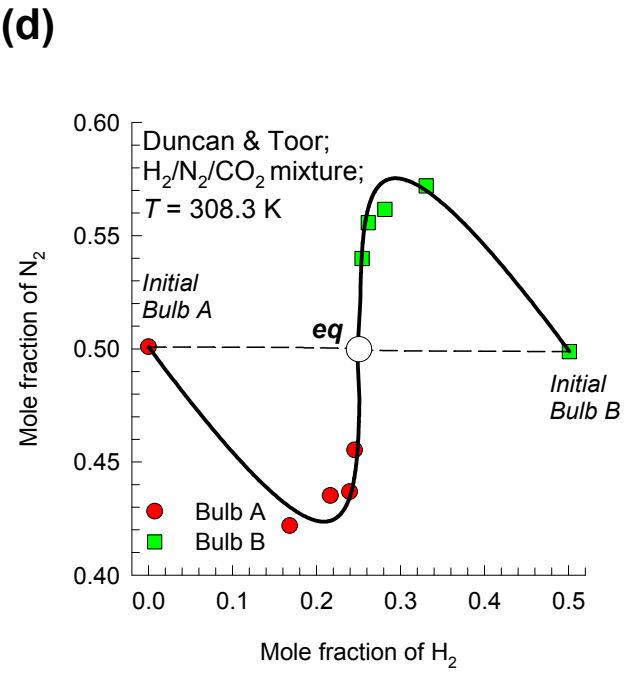
(d)
Duncan & Toor;
$H_2/N_2/CO_2$ mixture;
T = 308.3 K
Initial Bulb A
eq
Initial Bulb B
Bulb A
Bulb B
Mole fraction of N_2
Mole fraction of H_2

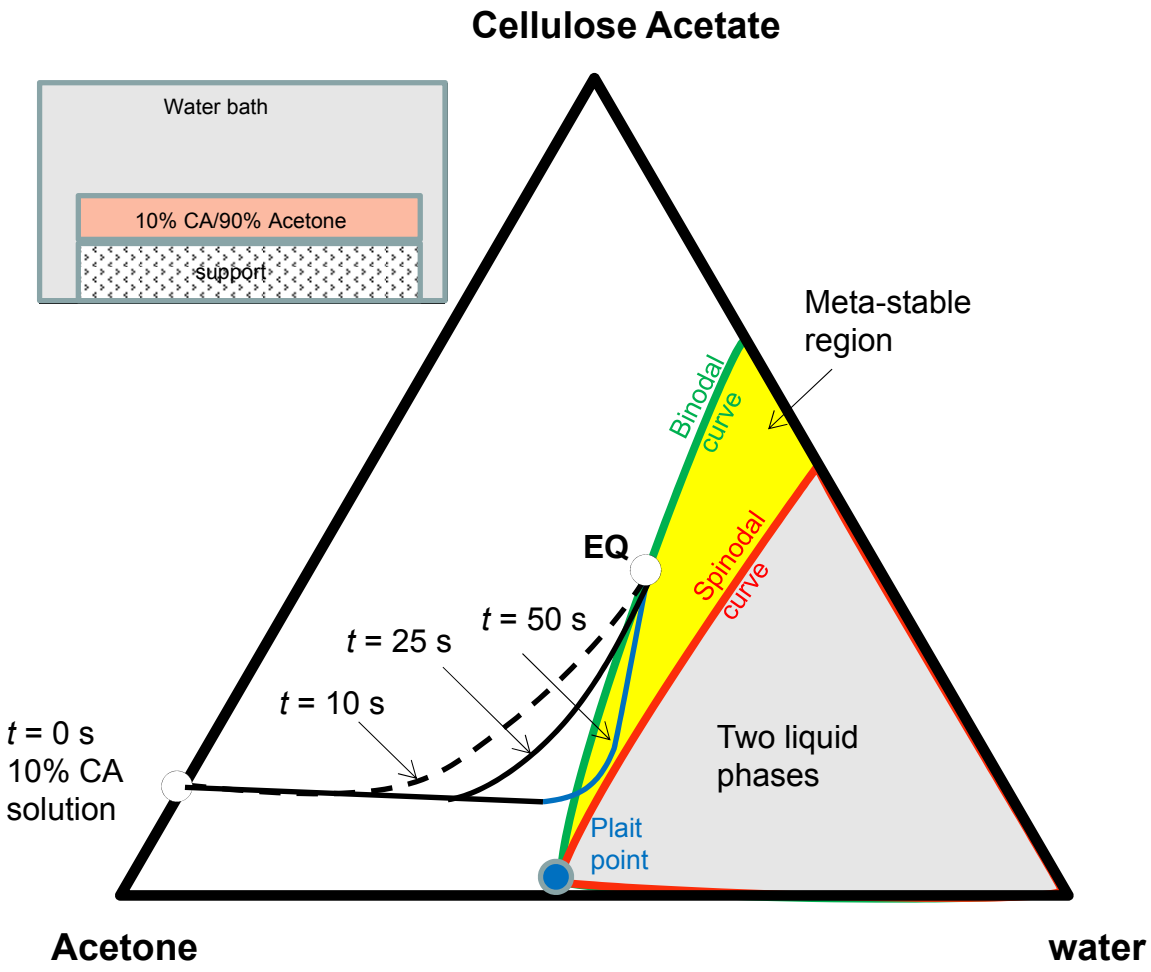
Cellulose Acetate
Water bath
10% CA/90% Acetone
support
Meta-stable region
Binodal curve
Spinodal curve
EQ
t = 50 s
t = 25 s
t = 10 s
t = 0 s
10% CA
solution
Two liquid phases
Plait point
Acetone
water

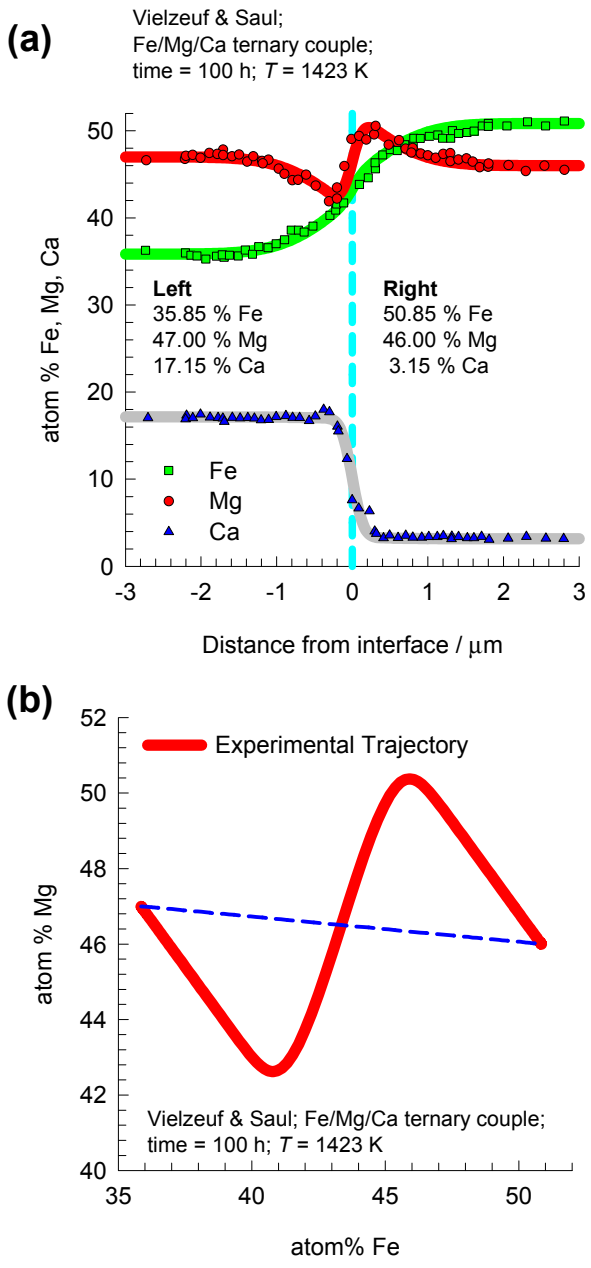
(a)
Vielzeuf & Saul;
Fe/Mg/Ca ternary couple;
time = 100 h; T = 1423 K
atom % Fe, Mg, Ca
Left
35.85 % Fe
47.00 % Mg
17.15 % Ca
Right
50.85 % Fe
46.00 % Mg
3.15 % Ca
Fe
Mg
Ca
Distance from interface / μm
(b)
Experimental Trajectory
atom % Mg
Vielzeuf & Saul; Fe/Mg/Ca ternary couple;
time = 100 h; T = 1423 K
atom% Fe

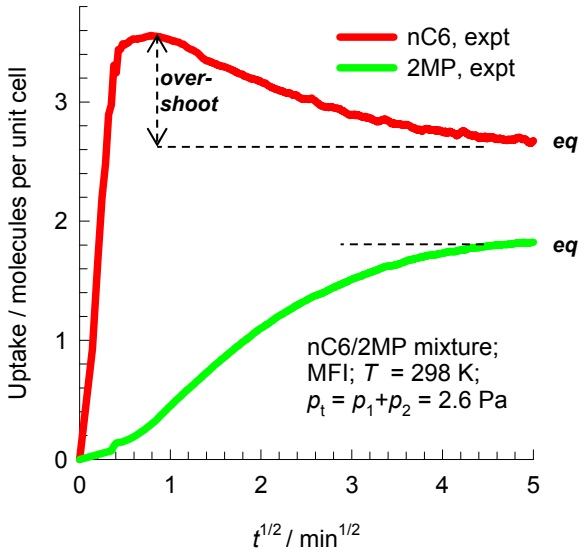
nC6, expt
2MP, expt
over-
shoot
eq
eq
nC6/2MP mixture;
MFI; T = 298 K;
$p_t = p_1 + p_2$ = 2.6 Pa
Uptake / molecules per unit cell
$t^{1/2}$ / $min^{1/2}$
0
1
2
3
4
5

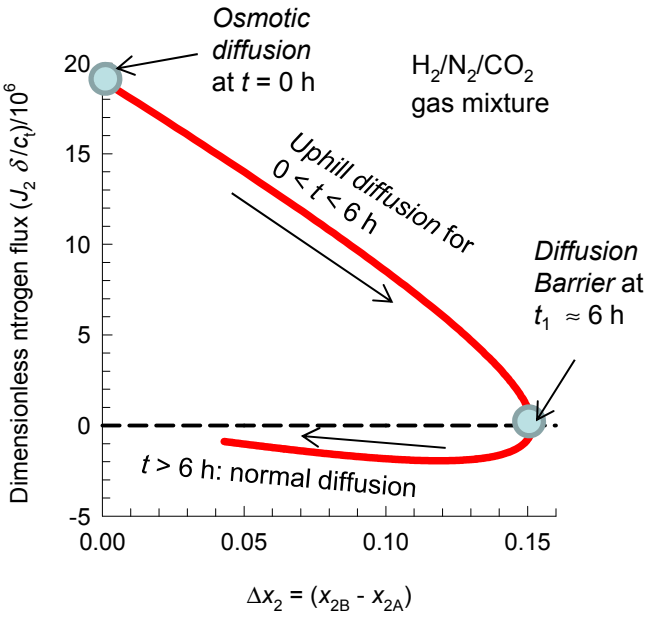
Osmotic diffusion at t = 0 h
H2/N2/CO2 gas mixture
Uphill diffusion for 0 < t < 6 h
Diffusion Barrier at t1 ≈ 6 h
t > 6 h: normal diffusion
Dimensionless ntrogen flux (J2 δ/c1)/10^6
Δx2 = (x2B - x2A)
20
15
10
5
0
-5
0.00
0.05
0.10
0.15

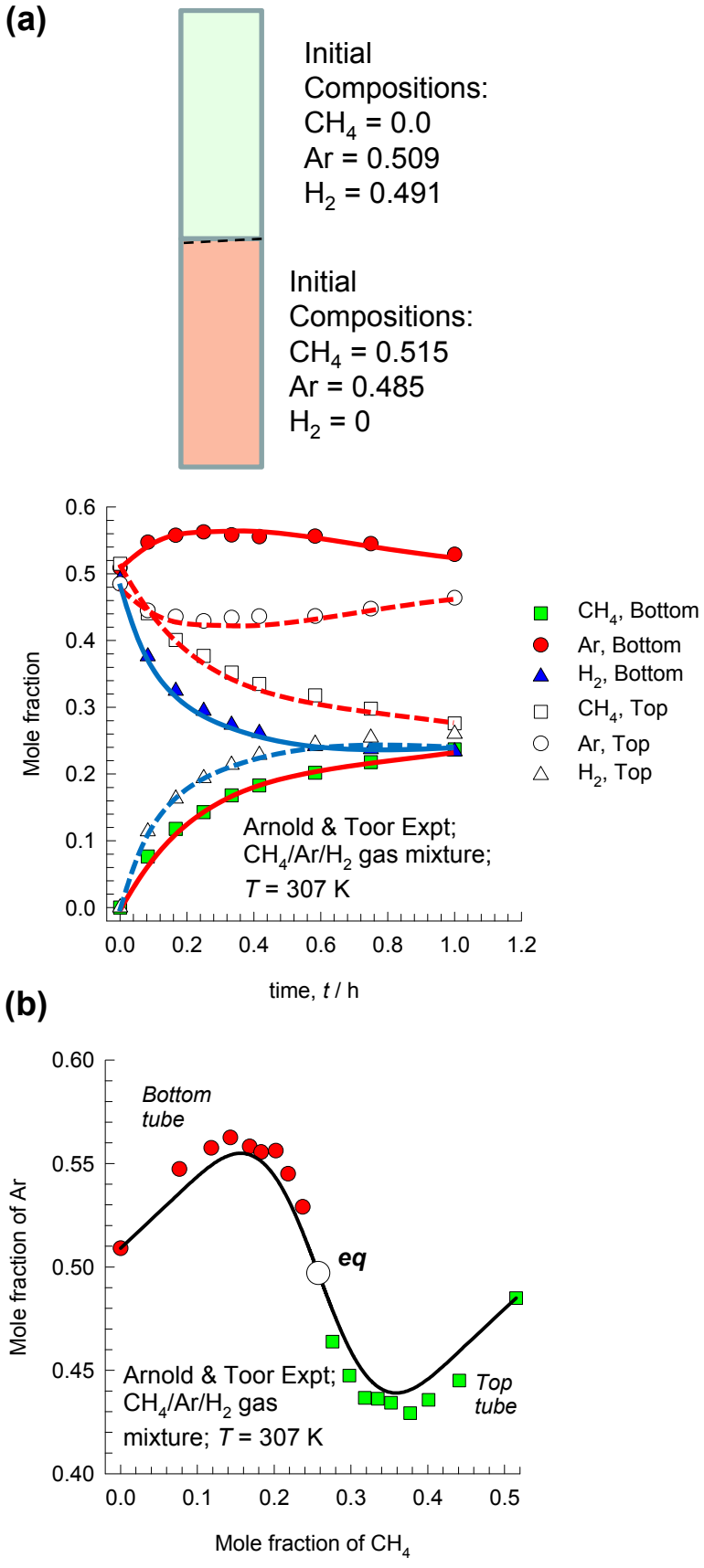
(a)
Initial Compositions:
CH4 = 0.0
Ar = 0.509
H2 = 0.491
Initial Compositions:
CH4 = 0.515
Ar = 0.485
H2 = 0
Mole fraction
time, t / h
CH4, Bottom
Ar, Bottom
H2, Bottom
CH4, Top
Ar, Top
H2, Top
Arnold & Toor Expt;
CH4/Ar/H2 gas mixture;
T = 307 K
(b)
Mole fraction of Ar
Mole fraction of CH4
Bottom tube
eq
Top tube
Arnold & Toor Expt;
CH4/Ar/H2 gas
mixture; T = 307 K

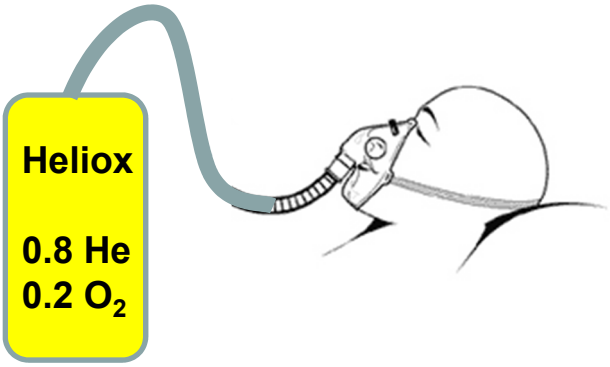
Heliox
0.8 He
0.2 O2

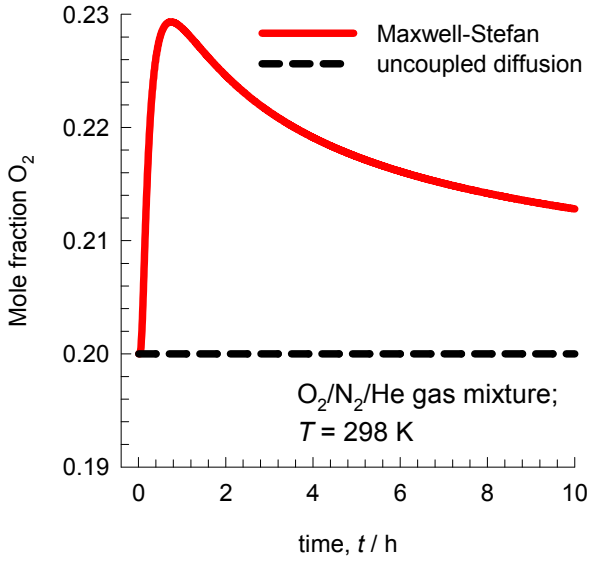
0.23
0.22
0.21
0.20
0.19
Mole fraction O2
Maxwell-Stefan
uncoupled diffusion
O2/N2/He gas mixture;
T = 298 K
0
2
4
6
8
10
time, t / h

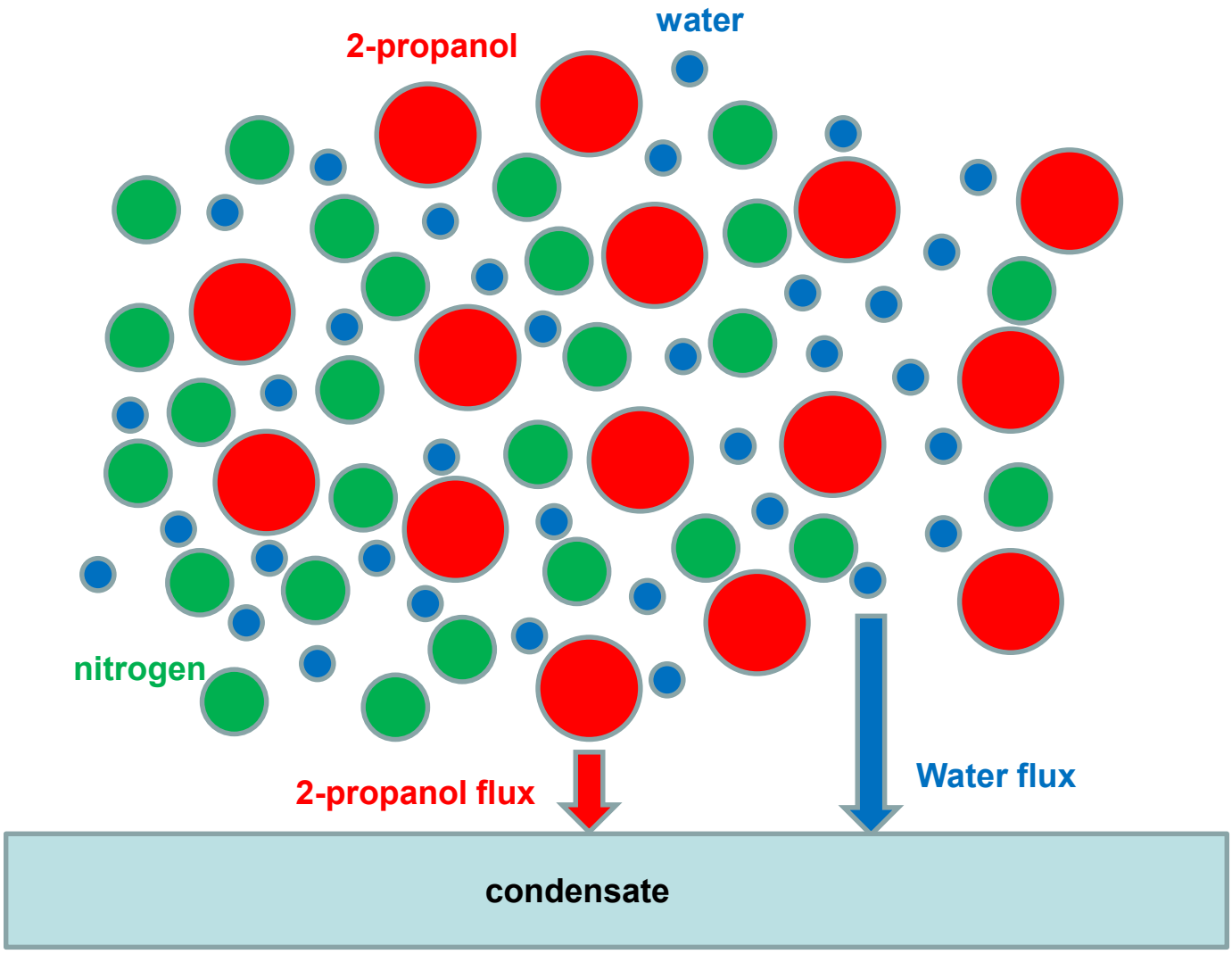
water
2-propanol
nitrogen
2-propanol flux
Water flux
condensate

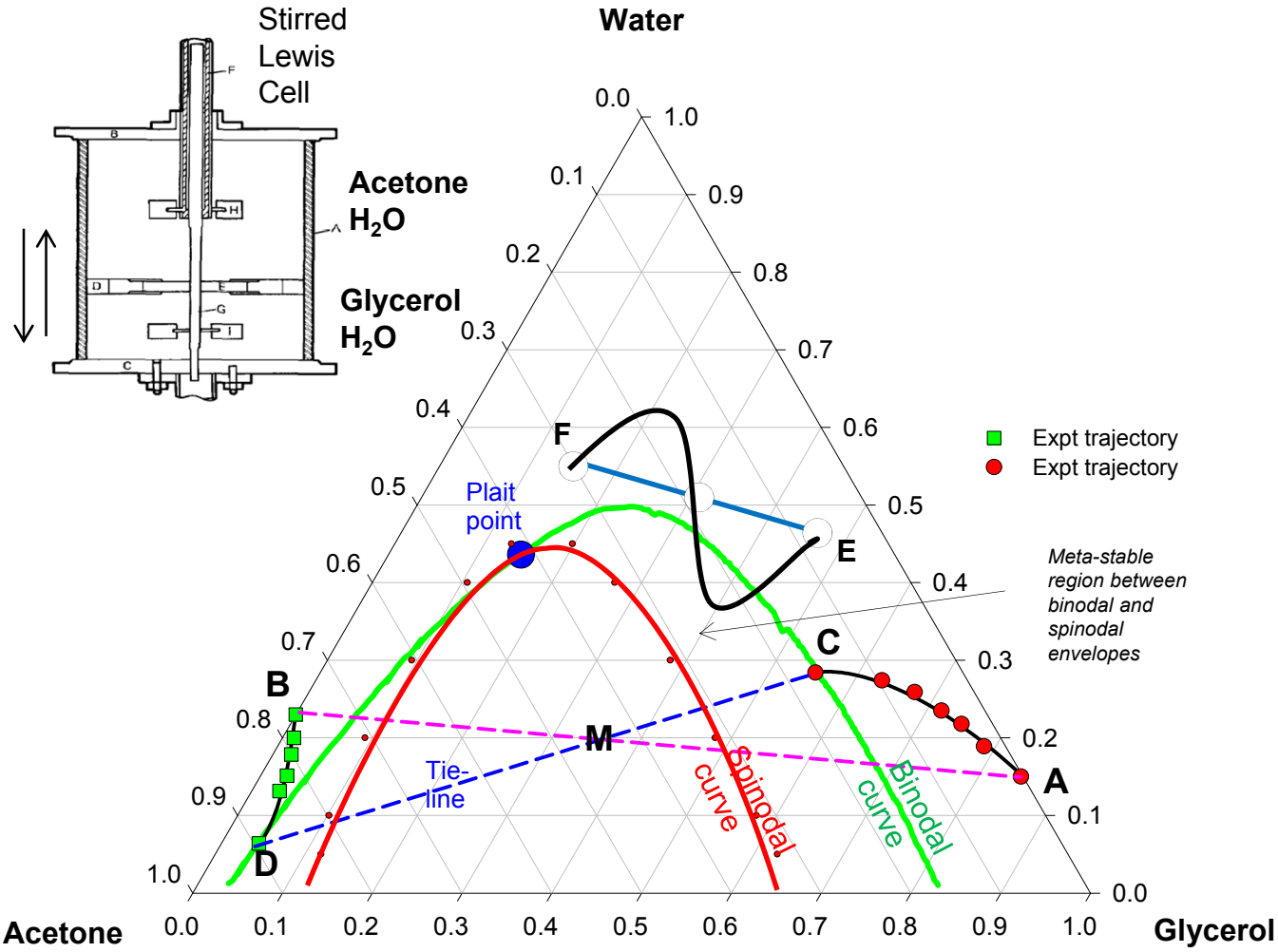
Stirred
Lewis
Cell
Acetone
H_2O
Glycerol
H_2O
Water
Acetone
Glycerol
Plait
point
Tie-
line
Spinodal
curve
Binodal
curve
Meta-stable
region between
binodal and
spinodal
envelopes
Expt trajectory
Expt trajectory
A
B
C
D
E
F
M

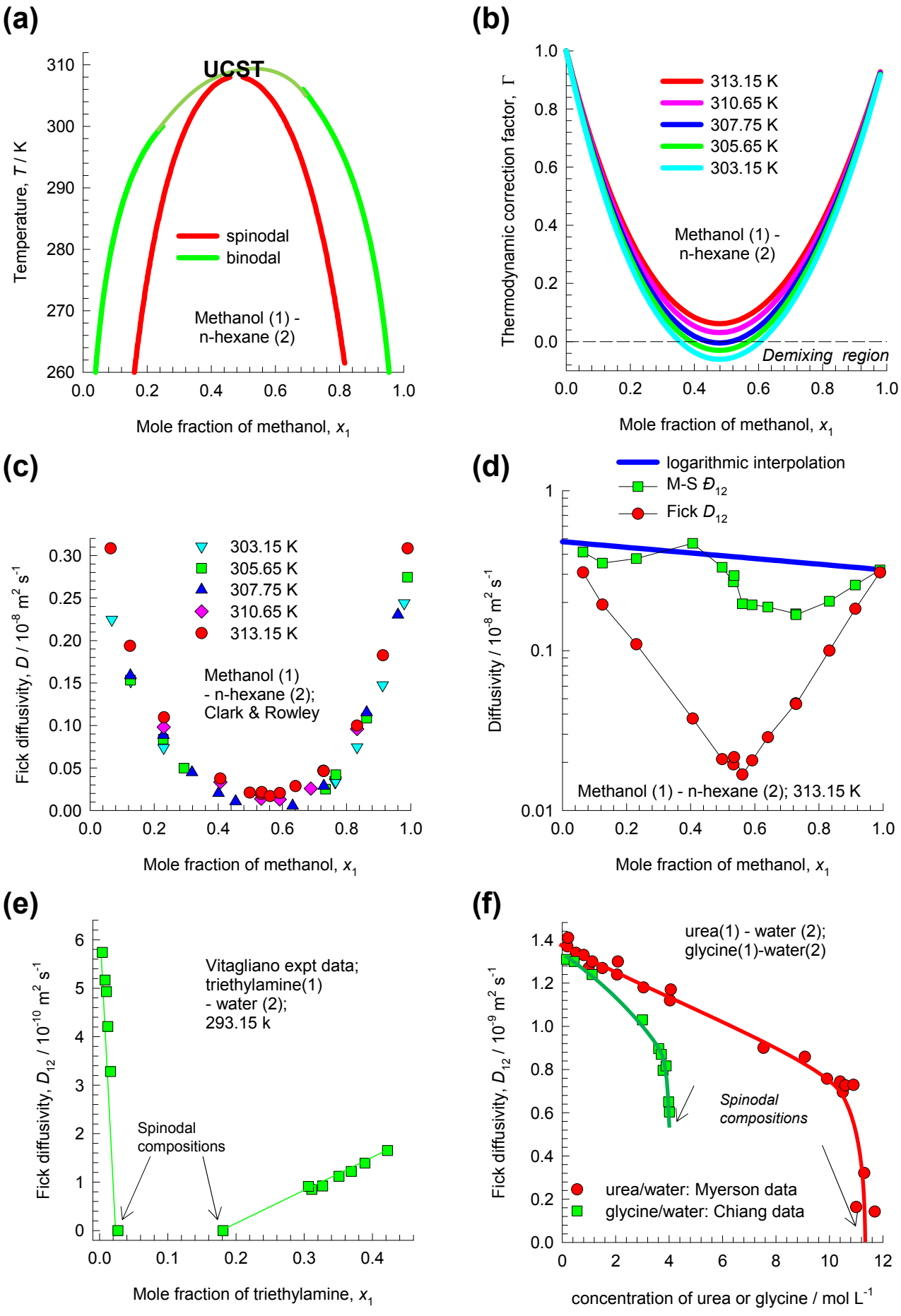
(a)
UCST
spinodal
binodal
Methanol (1) -
n-hexane (2)
Temperature, T / K
Mole fraction of methanol, x1
(b)
313.15 K
310.65 K
307.75 K
305.65 K
303.15 K
Methanol (1) -
n-hexane (2)
Demixing region
Thermodynamic correction factor, Γ
Mole fraction of methanol, x1
(c)
303.15 K
305.65 K
307.75 K
310.65 K
313.15 K
Methanol (1)
- n-hexane (2);
Clark & Rowley
Fick diffusivity, D / 10-8 m2 s-1
Mole fraction of methanol, x1
(d)
logarithmic interpolation
M-S Đ12
Fick D12
Methanol (1) - n-hexane (2); 313.15 K
Diffusivity / 10-8 m2 s-1
Mole fraction of methanol, x1
(e)
Vitagliano expt data;
triethylamine(1)
- water (2);
293.15 k
Spinodal
compositions
Fick diffusivity, D12 / 10-10 m2 s-1
Mole fraction of triethylamine, x1
(f)
urea(1) - water (2);
glycine(1)-water(2)
Spinodal
compositions
urea/water: Myerson data
glycine/water: Chiang data
Fick diffusivity, D12 / 10-9 m2 s-1
concentration of urea or glycine / mol L-1

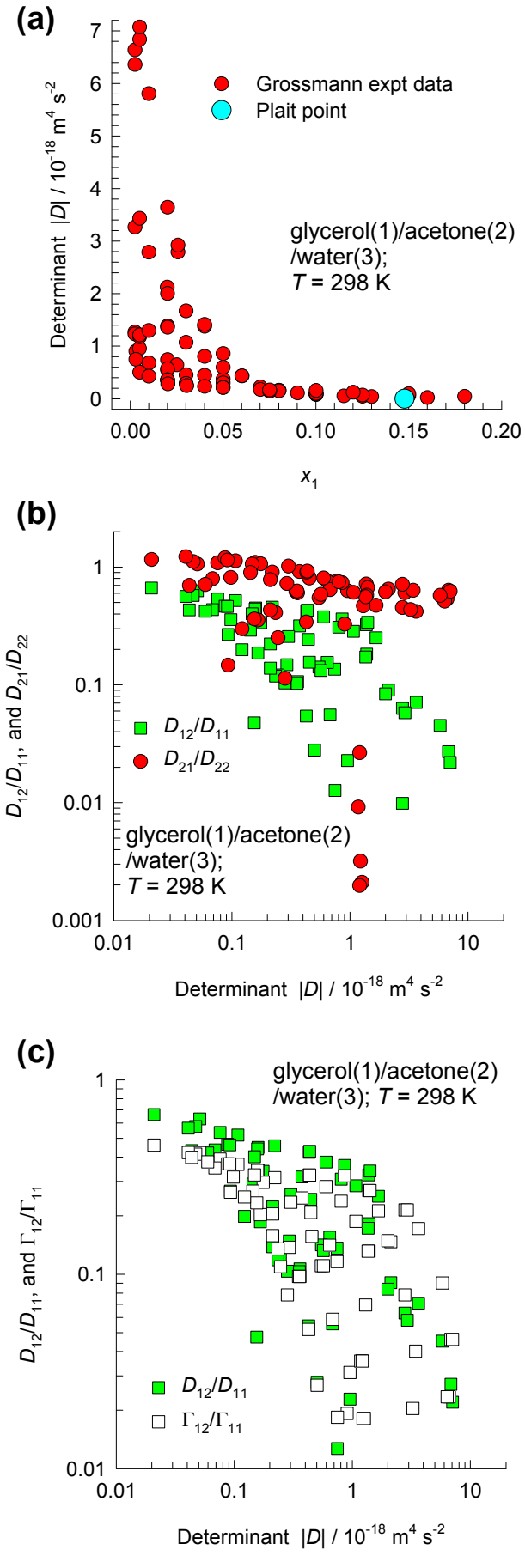
(a)
Determinant |D| / 10^-18 m^4 s^-2
Grossmann expt data
Plait point
glycerol(1)/acetone(2)
/water(3);
T = 298 K
x1
(b)
D12/D11, and D21/D22
D12/D11
D21/D22
glycerol(1)/acetone(2)
/water(3);
T = 298 K
Determinant |D| / 10^-18 m^4 s^-2
(c)
glycerol(1)/acetone(2)
/water(3); T = 298 K
D12/D11, and Γ12/Γ11
D12/D11
Γ12/Γ11
Determinant |D| / 10^-18 m^4 s^-2

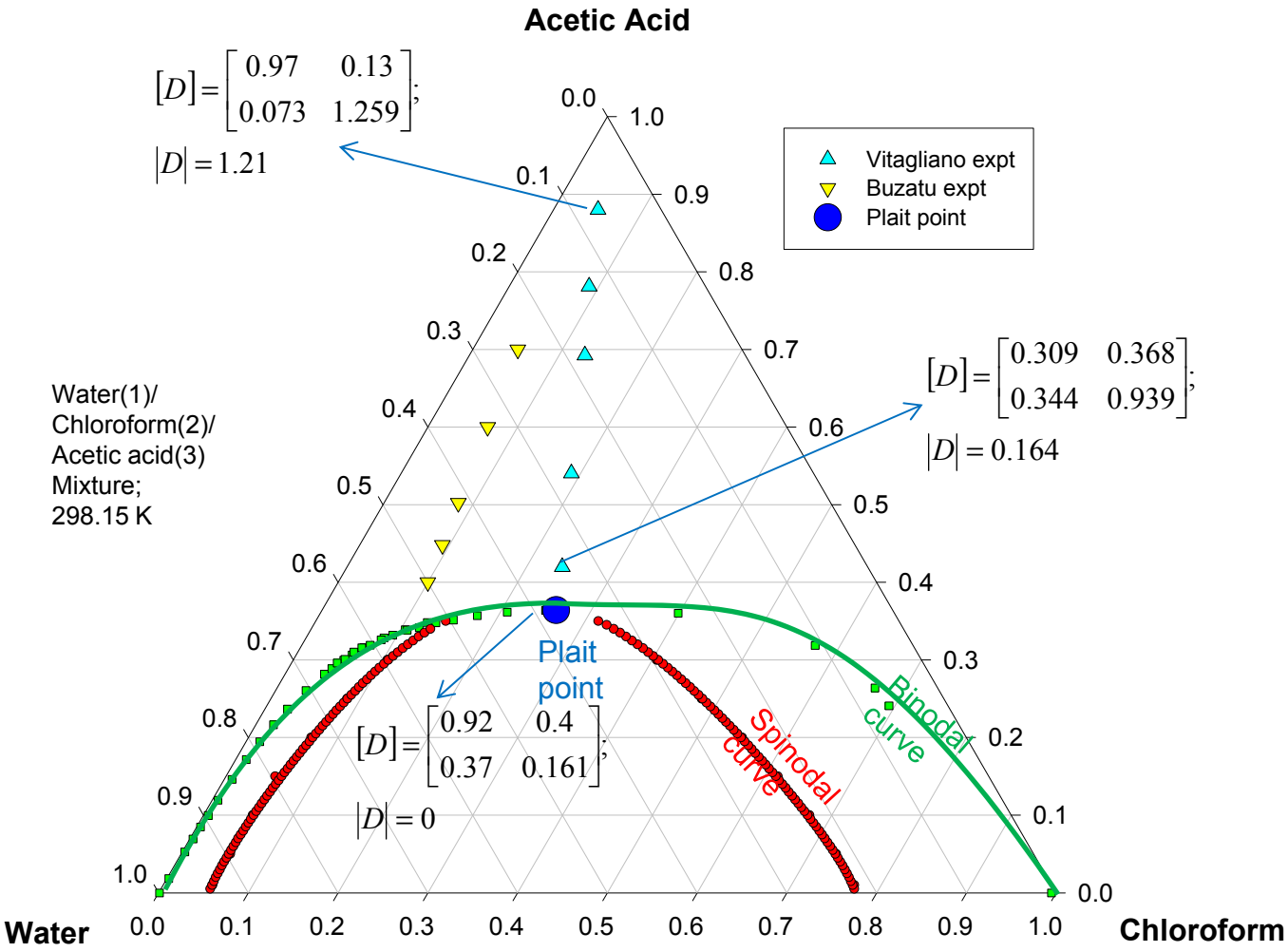
Acetic Acid
$[D]=\begin{bmatrix}0.97 & 0.13\\ 0.073 & 1.259\end{bmatrix}$;
$|D|=1.21$
Vitagliano expt
Buzatu expt
Plait point
Water(1)/
Chloroform(2)/
Acetic acid(3)
Mixture;
298.15 K
$[D]=\begin{bmatrix}0.309 & 0.368\\ 0.344 & 0.939\end{bmatrix}$;
$|D|=0.164$
Plait
point
$[D]=\begin{bmatrix}0.92 & 0.4\\ 0.37 & 0.161\end{bmatrix}$;
$|D|=0$
Spinodal
curve
Binodal
curve
Water
Chloroform

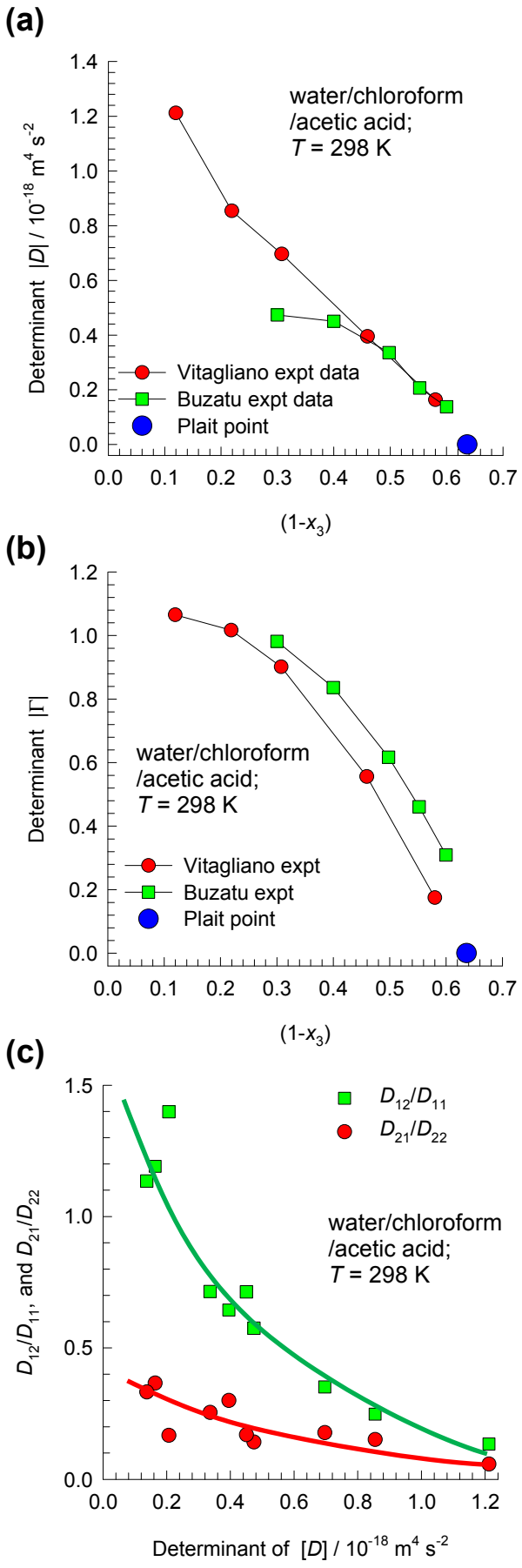
(a)
water/chloroform
/acetic acid;
T = 298 K
Vitagliano expt data
Buzatu expt data
Plait point
Determinant |D| / 10^-18 m^4 s^-2
(1-x3)
(b)
water/chloroform
/acetic acid;
T = 298 K
Vitagliano expt
Buzatu expt
Plait point
Determinant |Γ|
(1-x3)
(c)
D12/D11
D21/D22
water/chloroform
/acetic acid;
T = 298 K
D12/D11, and D21/D22
Determinant of [D] / 10^-18 m^4 s^-2

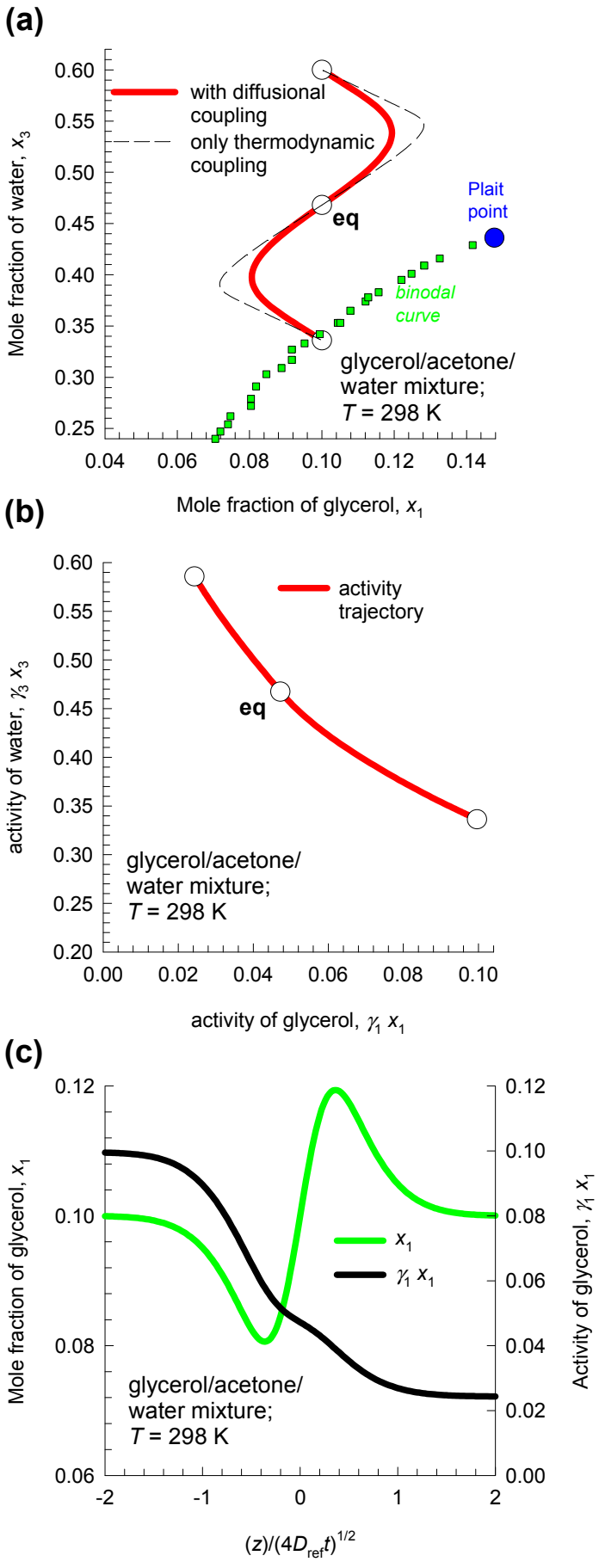
(a)
with diffusional coupling
only thermodynamic coupling
eq
Plait point
binodal curve
glycerol/acetone/ water mixture; T = 298 K
Mole fraction of water, x3
Mole fraction of glycerol, x1
(b)
activity trajectory
eq
glycerol/acetone/ water mixture; T = 298 K
activity of water, γ3 x3
activity of glycerol, γ1 x1
(c)
x1
γ1 x1
glycerol/acetone/ water mixture; T = 298 K
Mole fraction of glycerol, x1
Activity of glycerol, γ1 x1
(z)/(4Dref t)1/2

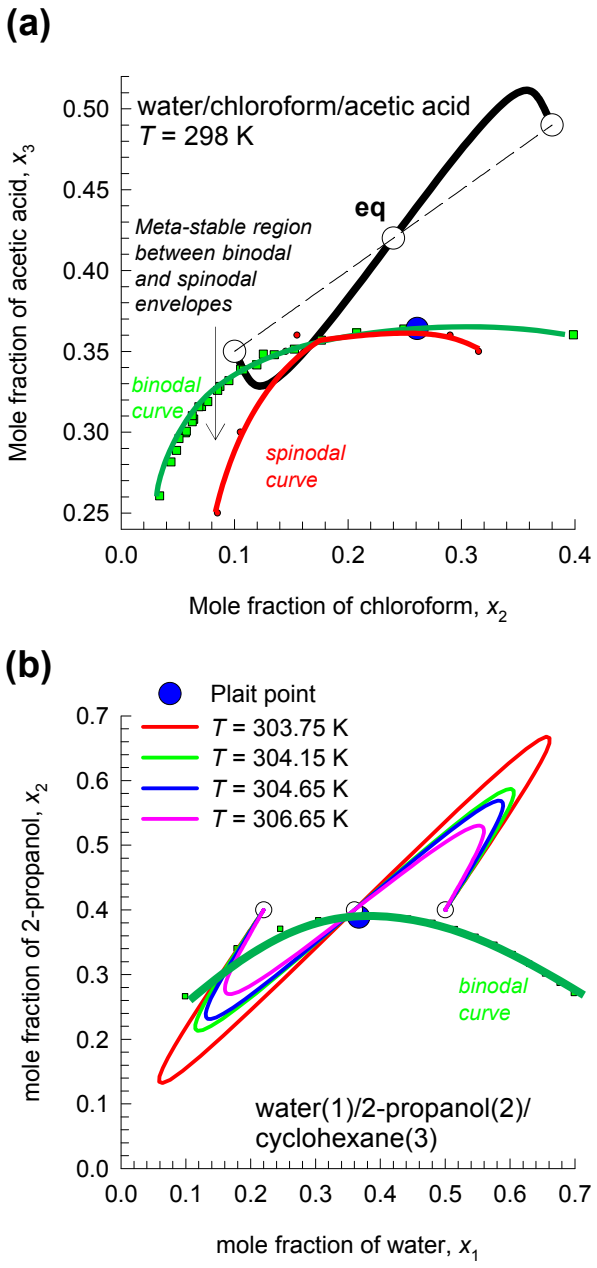
(a)
water/chloroform/acetic acid
T = 298 K
eq
Meta-stable region
between binodal
and spinodal
envelopes
binodal
curve
spinodal
curve
Mole fraction of acetic acid, x3
Mole fraction of chloroform, x2
0.50
0.45
0.40
0.35
0.30
0.25
0.0
0.1
0.2
0.3
0.4
(b)
Plait point
T = 303.75 K
T = 304.15 K
T = 304.65 K
T = 306.65 K
binodal
curve
water(1)/2-propanol(2)/
cyclohexane(3)
mole fraction of 2-propanol, x2
mole fraction of water, x1
0.7
0.6
0.5
0.4
0.3
0.2
0.1
0.0

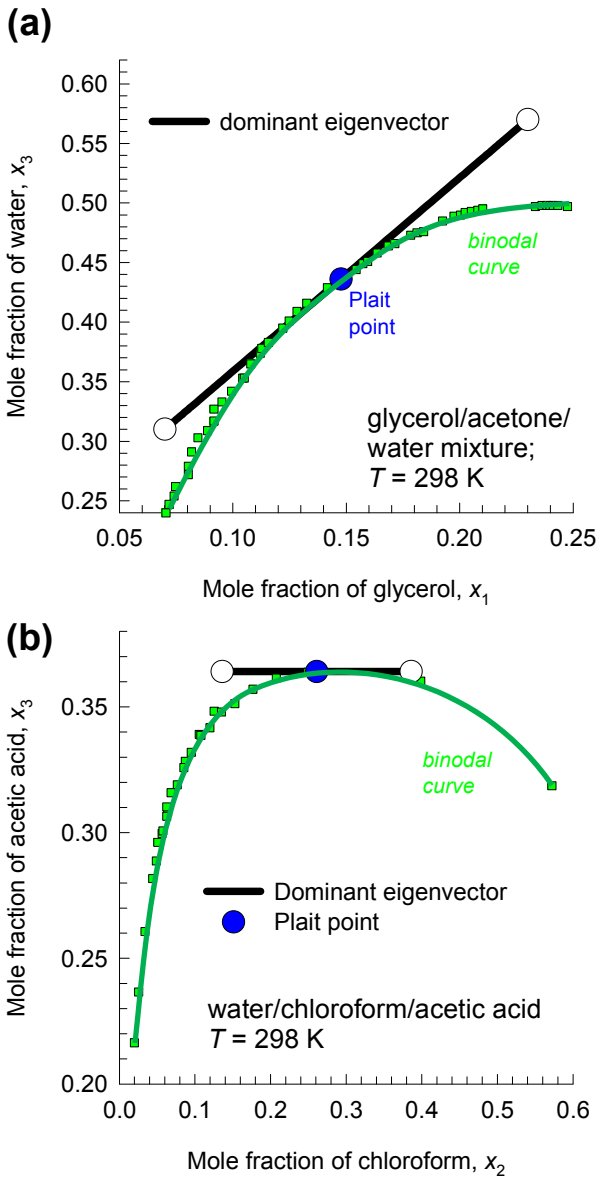
(a)
dominant eigenvector
binodal curve
Plait point
glycerol/acetone/
water mixture;
T = 298 K
Mole fraction of water, x3
Mole fraction of glycerol, x1
0.60
0.55
0.50
0.45
0.40
0.35
0.30
0.25
0.05
0.10
0.15
0.20
0.25
(b)
binodal curve
Dominant eigenvector
Plait point
water/chloroform/acetic acid
T = 298 K
Mole fraction of acetic acid, x3
Mole fraction of chloroform, x2
0.35
0.30
0.25
0.20
0.0
0.1
0.2
0.3
0.4
0.5
0.6

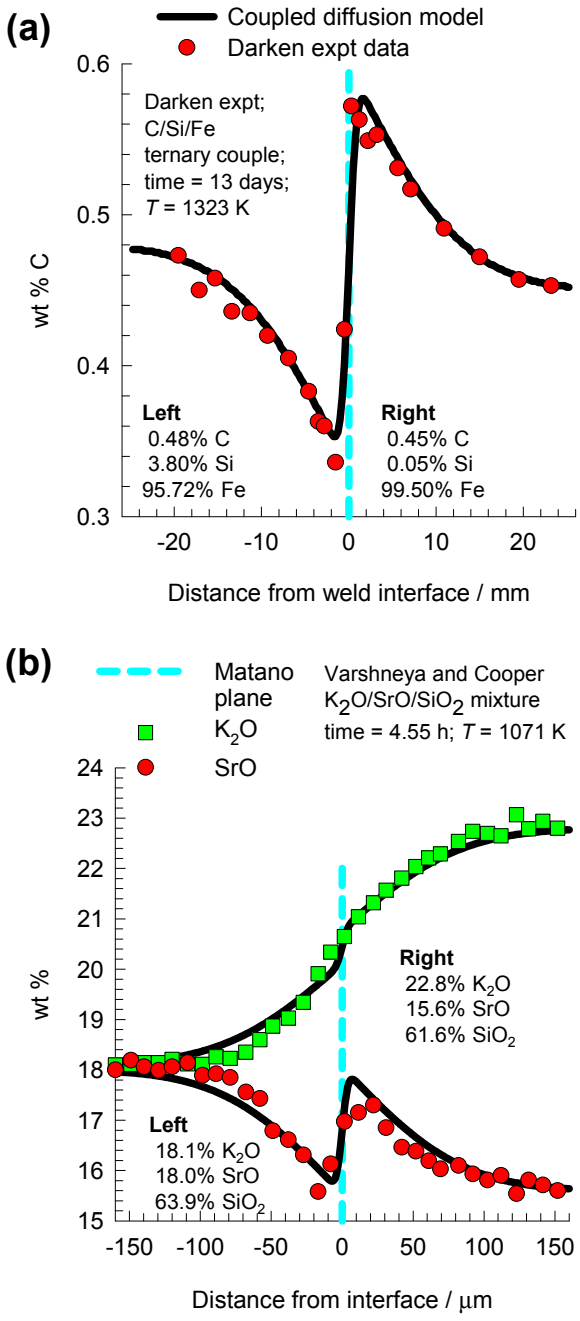
(a)
Coupled diffusion model
Darken expt data
Darken expt;
C/Si/Fe
ternary couple;
time = 13 days;
T = 1323 K
Left
0.48% C
3.80% Si
95.72% Fe
Right
0.45% C
0.05% Si
99.50% Fe
wt % C
Distance from weld interface / mm
(b)
Matano plane
K2O
SrO
Varshneya and Cooper
K2O/SrO/SiO2 mixture
time = 4.55 h; T = 1071 K
Right
22.8% K2O
15.6% SrO
61.6% SiO2
Left
18.1% K2O
18.0% SrO
63.9% SiO2
wt %
Distance from interface / μm

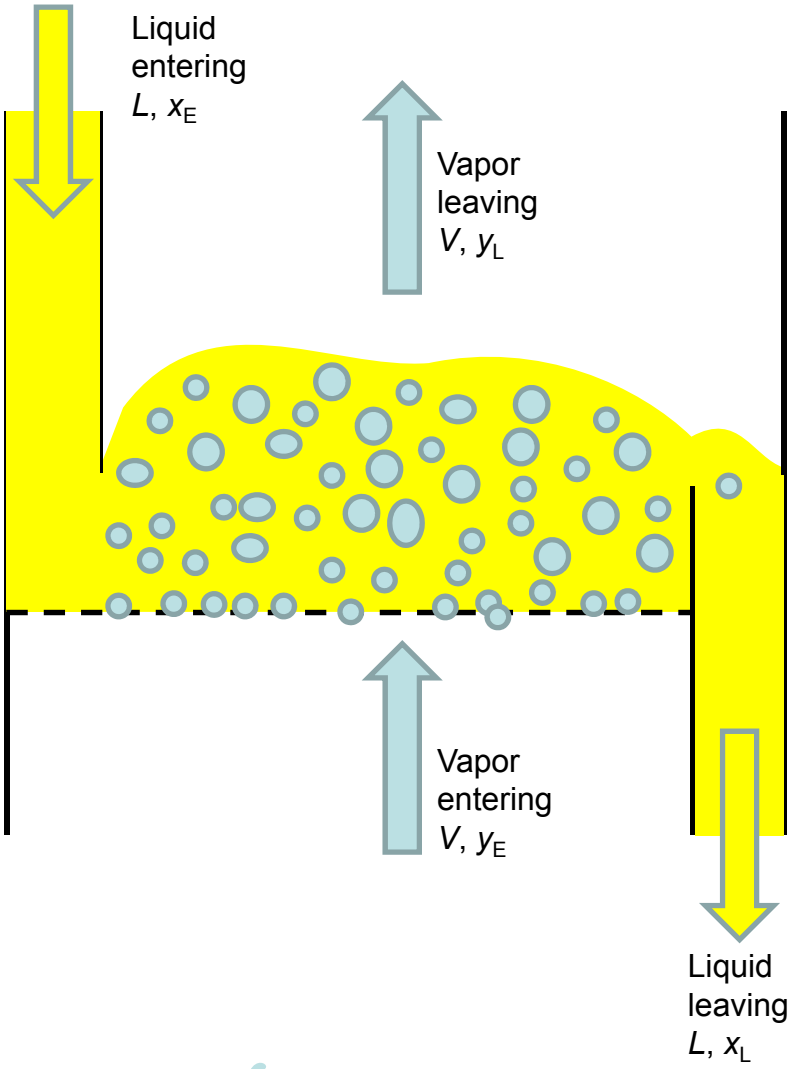

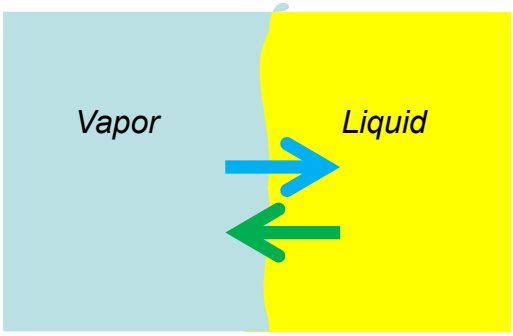

Diffusional coupling effects need to be accounted for in either phase

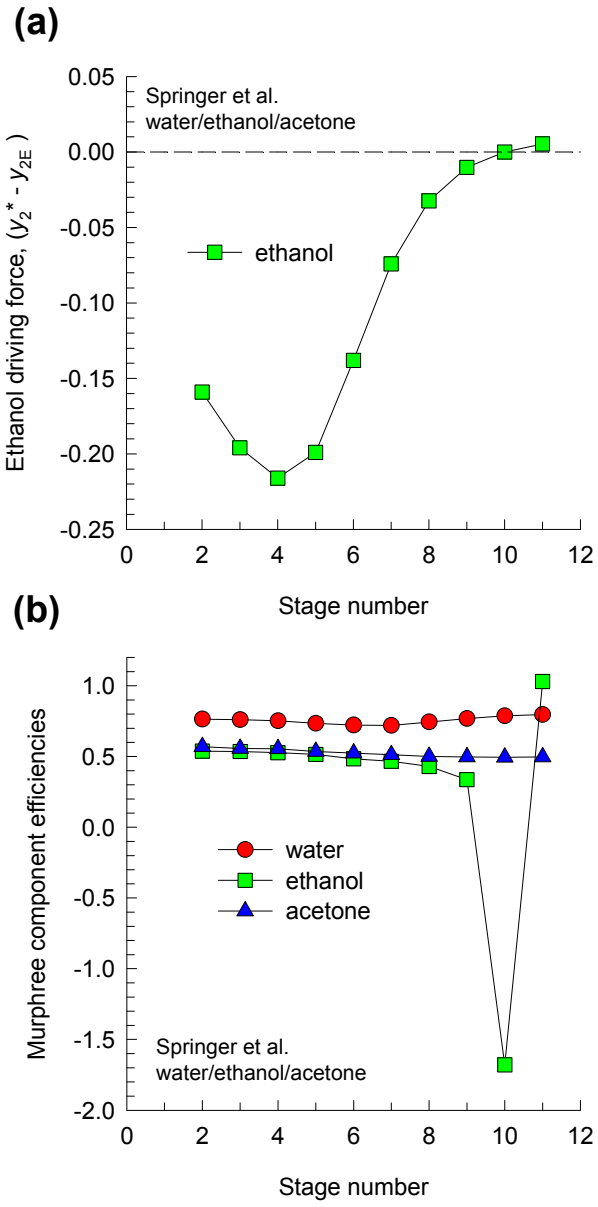
(a)
Springer et al.
water/ethanol/acetone
Ethanol driving force, (y_2^* - y_{2E})
ethanol
0.05
0.00
-0.05
-0.10
-0.15
-0.20
-0.25
0
2
4
6
8
10
12
Stage number
(b)
Murphree component efficiencies
water
ethanol
acetone
Springer et al.
water/ethanol/acetone
1.0
0.5
0.0
-0.5
-1.0
-1.5
-2.0
0
2
4
6
8
10
12
Stage number

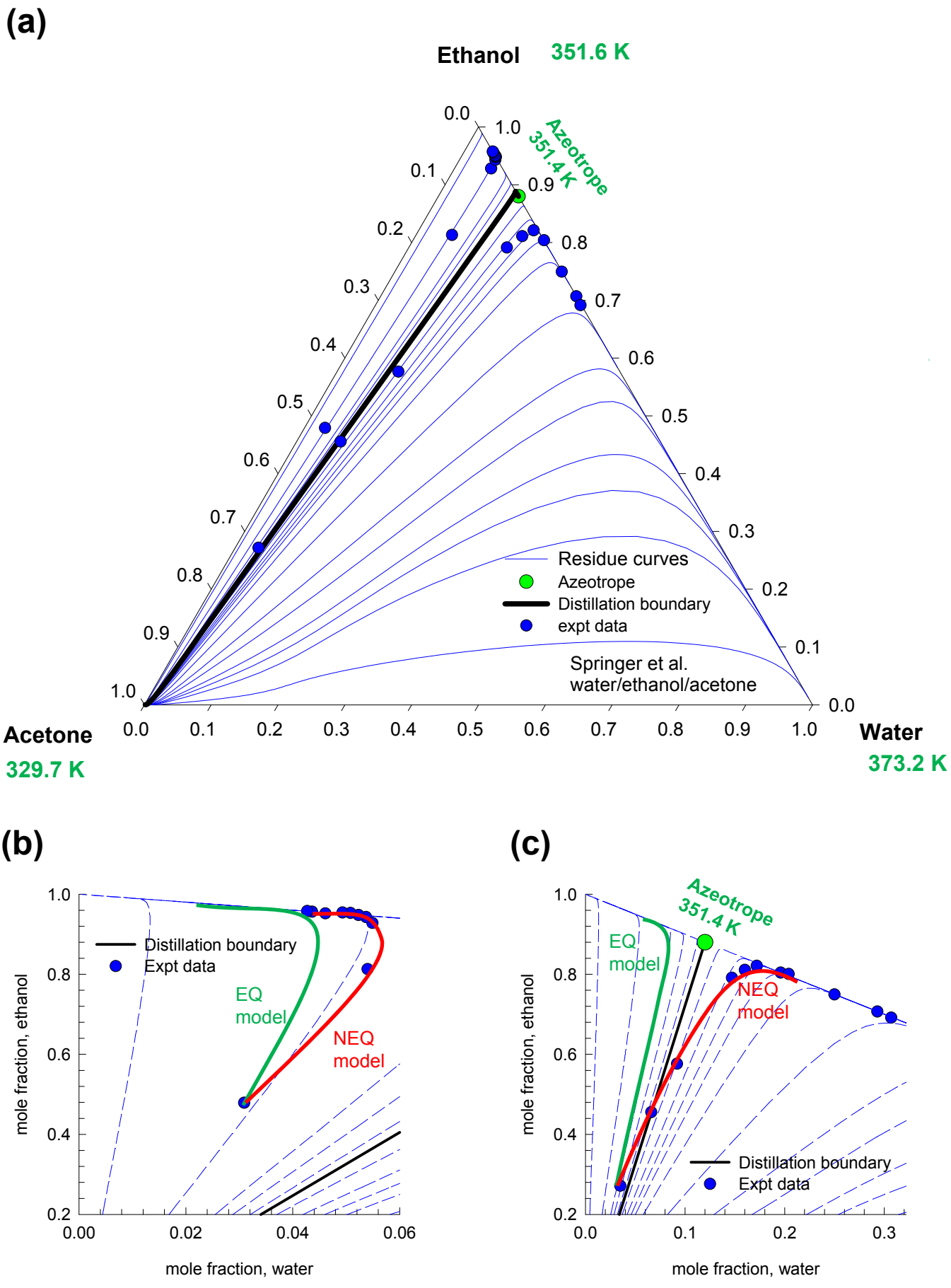
(a)
Ethanol
351.6 K
Azeotrope
351.4 K
Residue curves
Azeotrope
Distillation boundary
expt data
Springer et al.
water/ethanol/acetone
Acetone
329.7 K
Water
373.2 K
(b)
Distillation boundary
Expt data
EQ
model
NEQ
model
mole fraction, ethanol
mole fraction, water
(c)
Azeotrope
351.4 K
EQ
model
NEQ
model
Distillation boundary
Expt data
mole fraction, ethanol
mole fraction, water

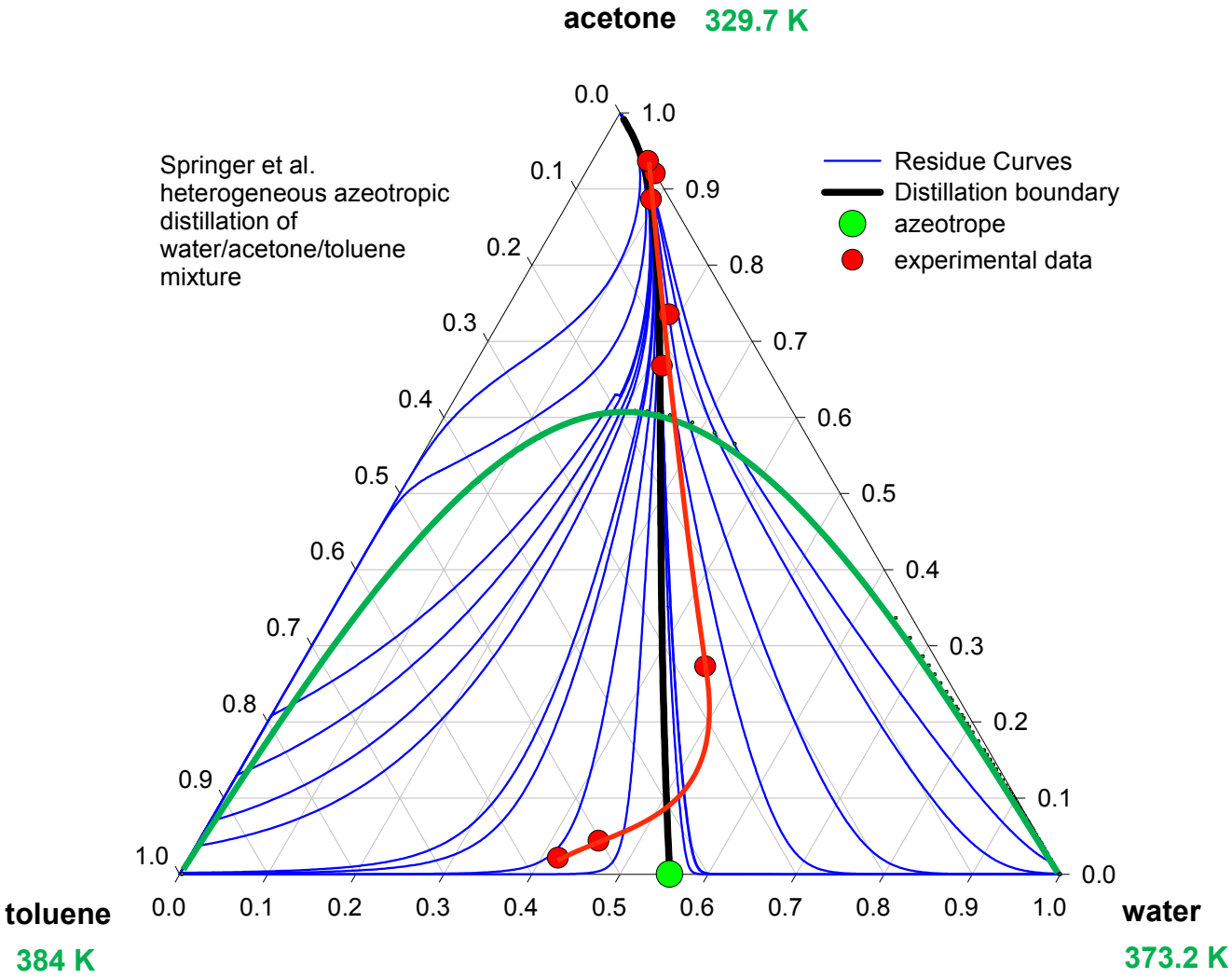
acetone
329.7 K
Springer et al.
heterogeneous azeotropic
distillation of
water/acetone/toluene
mixture
Residue Curves
Distillation boundary
azeotrope
experimental data
toluene
384 K
water
373.2 K
0.0
0.1
0.2
0.3
0.4
0.5
0.6
0.7
0.8
0.9
1.0

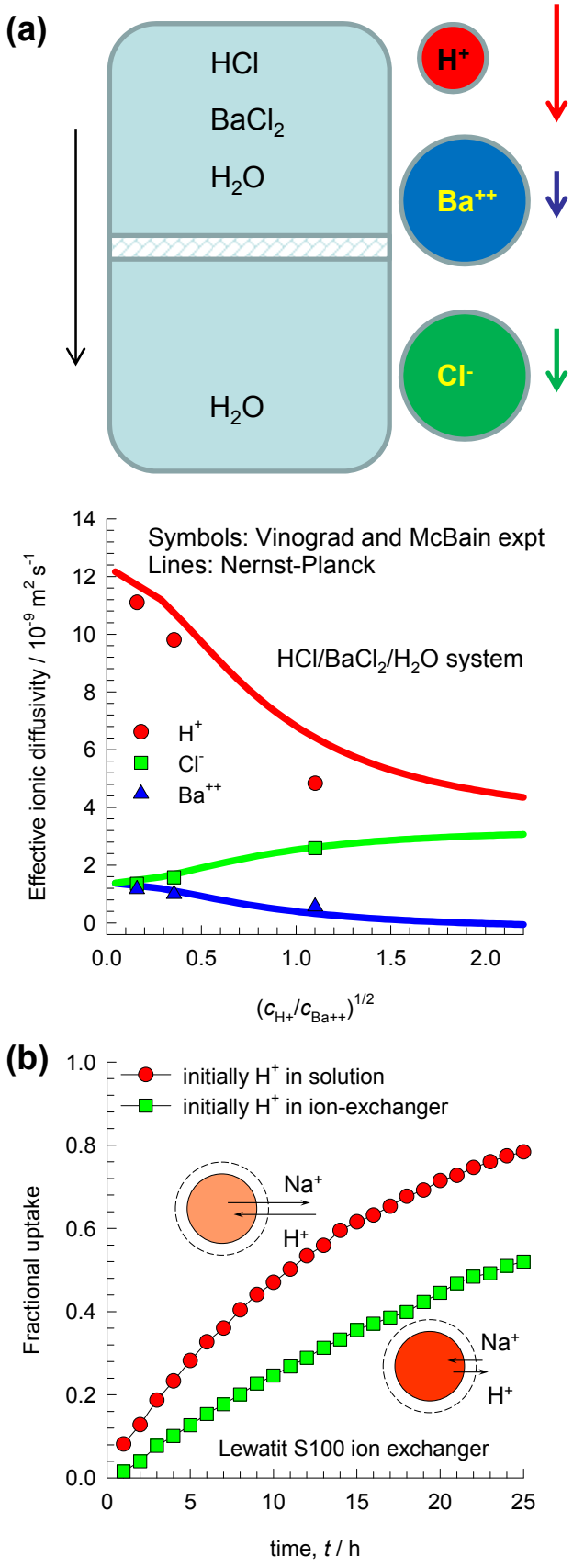
(a)
HCl
BaCl2
H2O
H2O
H+
Ba++
Cl-
Symbols: Vinograd and McBain expt
Lines: Nernst-Planck
HCl/BaCl2/H2O system
H+
Cl-
Ba++
Effective ionic diffusivity / 10-9 m2 s-1
(cH+/cBa++)1/2
(b)
initially H+ in solution
initially H+ in ion-exchanger
Na+
H+
Na+
H+
Lewatit S100 ion exchanger
Fractional uptake
time, t / h

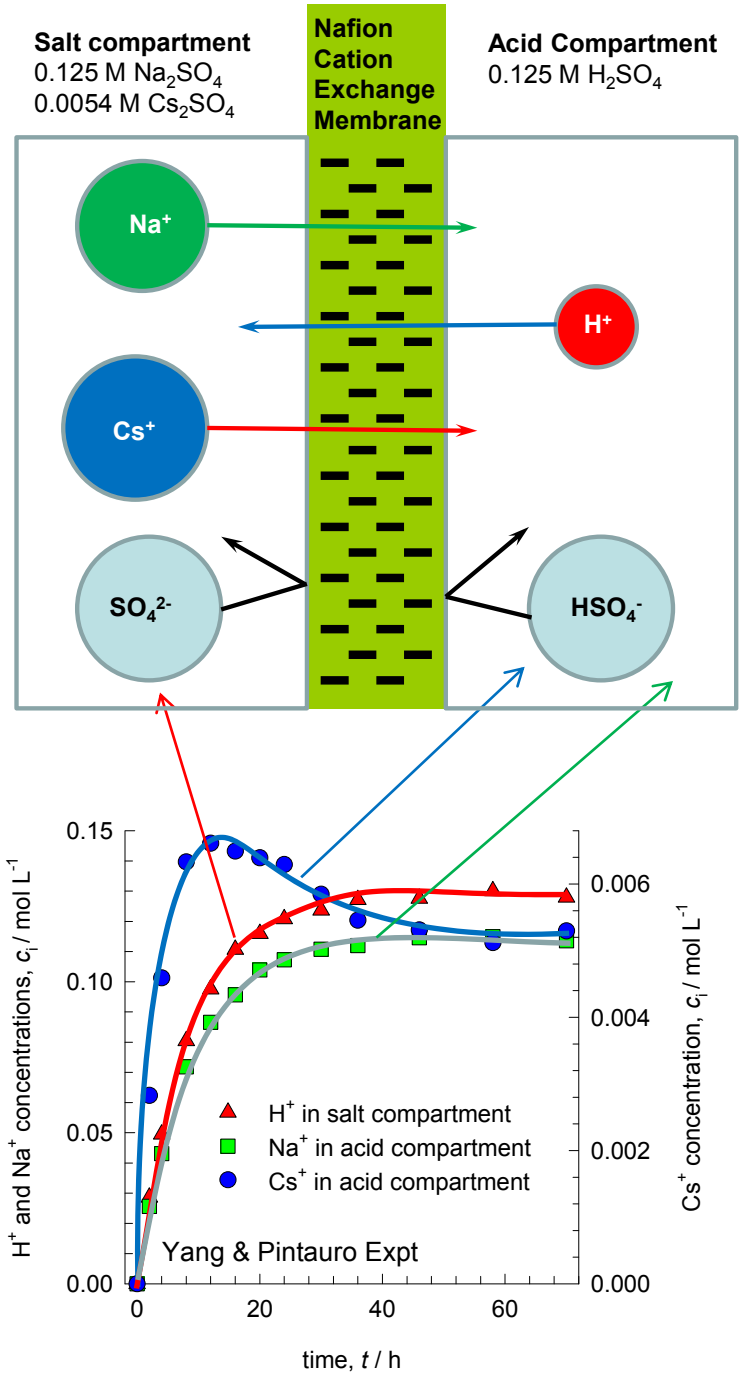
Salt compartment
0.125 M Na2SO4
0.0054 M Cs2SO4
Nafion Cation Exchange Membrane
Acid Compartment
0.125 M H2SO4
Na+
H+
Cs+
SO4 2-
HSO4-
0.15
0.10
0.05
0.00
0.006
0.004
0.002
0.000
0
20
40
60
H+ and Na+ concentrations, ci / mol L-1
Cs+ concentration, ci / mol L-1
time, t / h
H+ in salt compartment
Na+ in acid compartment
Cs+ in acid compartment
Yang & Pintauro Expt

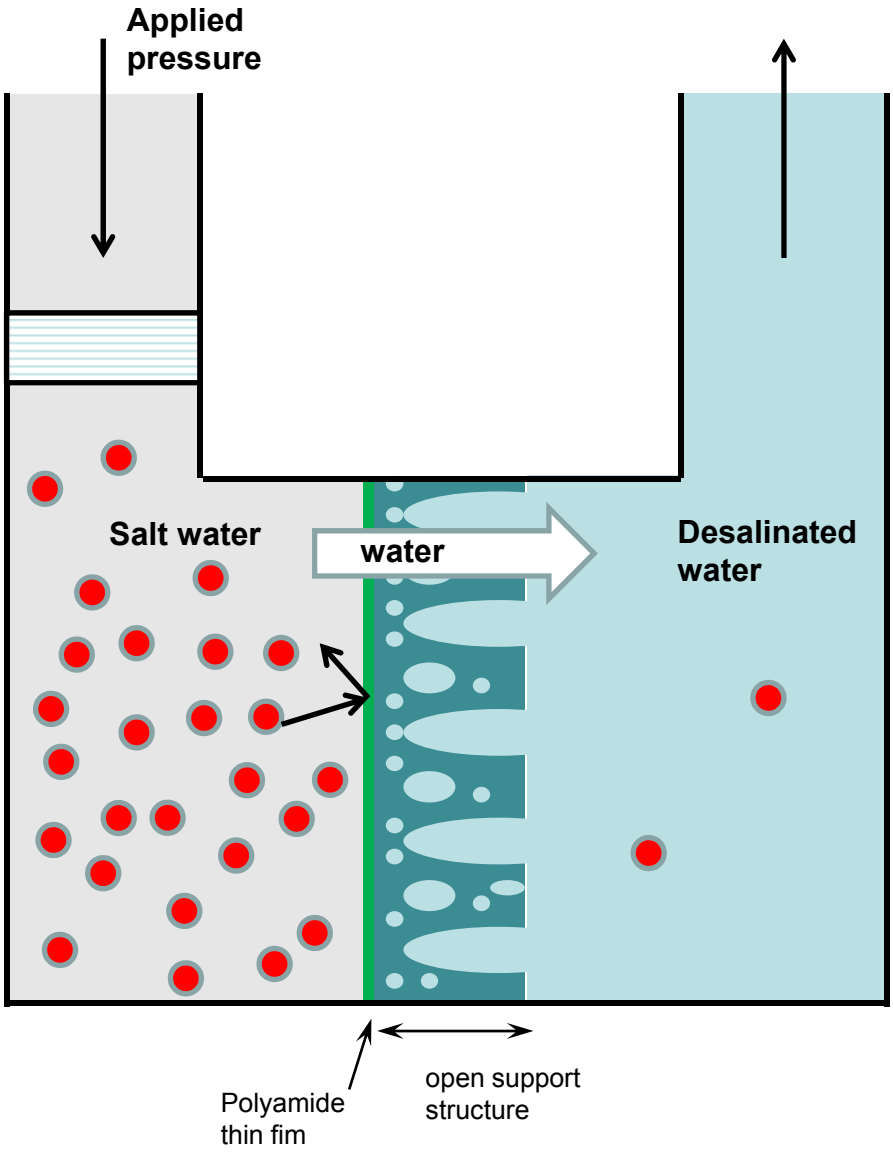
Applied
pressure
Salt water
water
Desalinated
water
Polyamide
thin fim
open support
structure

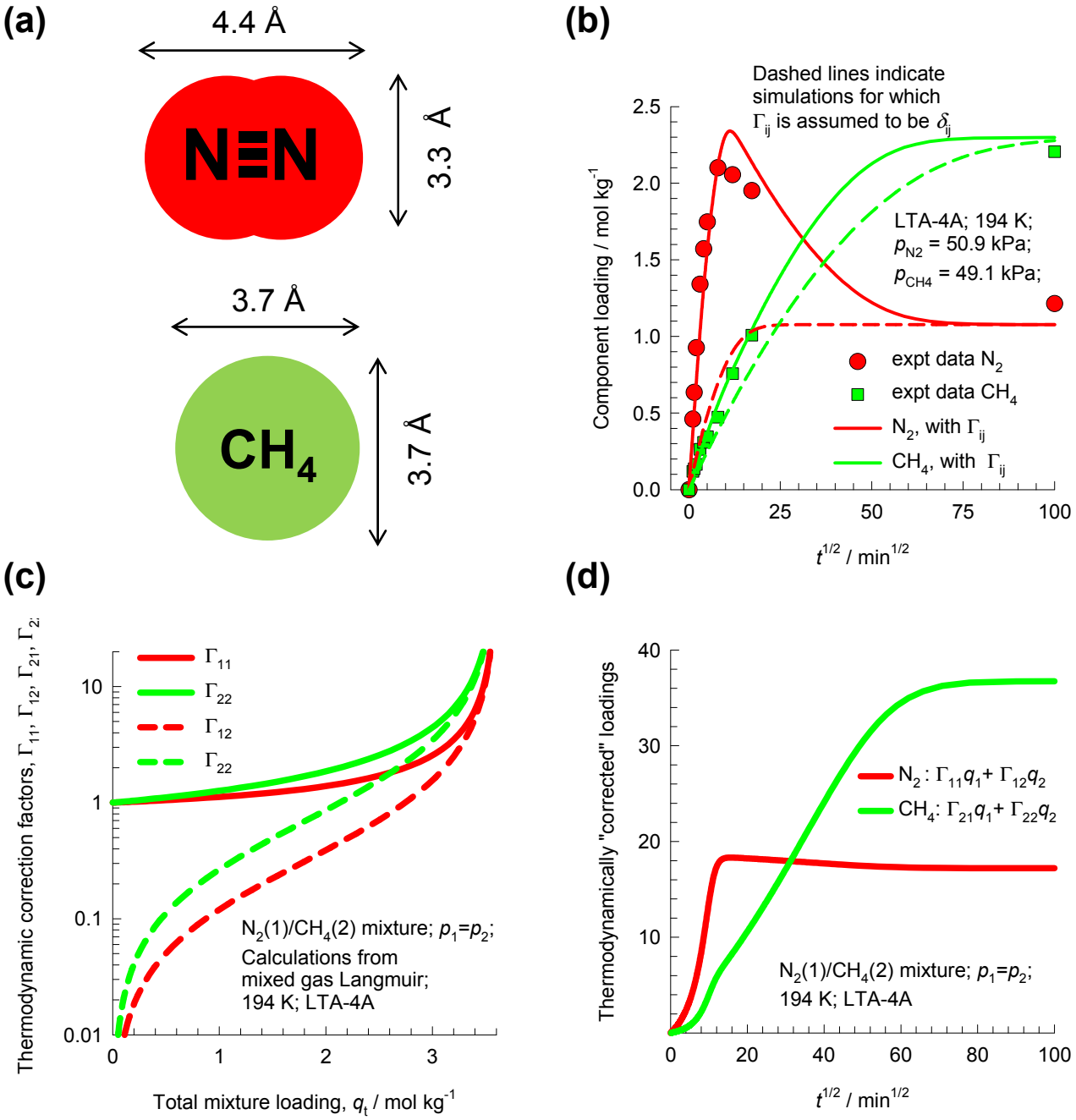
(a)
4.4 Å
N≡N
3.3 Å
3.7 Å
CH4
3.7 Å
(b)
Dashed lines indicate simulations for which Γij is assumed to be δij
LTA-4A; 194 K;
pN2 = 50.9 kPa;
pCH4 = 49.1 kPa;
expt data N2
expt data CH4
N2, with Γij
CH4, with Γij
Component loading / mol kg-1
t1/2 / min1/2
(c)
Γ11
Γ22
Γ12
Γ22
N2(1)/CH4(2) mixture; p1=p2;
Calculations from mixed gas Langmuir;
194 K; LTA-4A
Thermodynamic correction factors, Γ11, Γ12, Γ21, Γ2;
Total mixture loading, qt / mol kg-1
(d)
N2 : Γ11q1+ Γ12q2
CH4: Γ21q1+ Γ22q2
N2(1)/CH4(2) mixture; p1=p2;
194 K; LTA-4A
Thermodynamically "corrected" loadings
t1/2 / min1/2

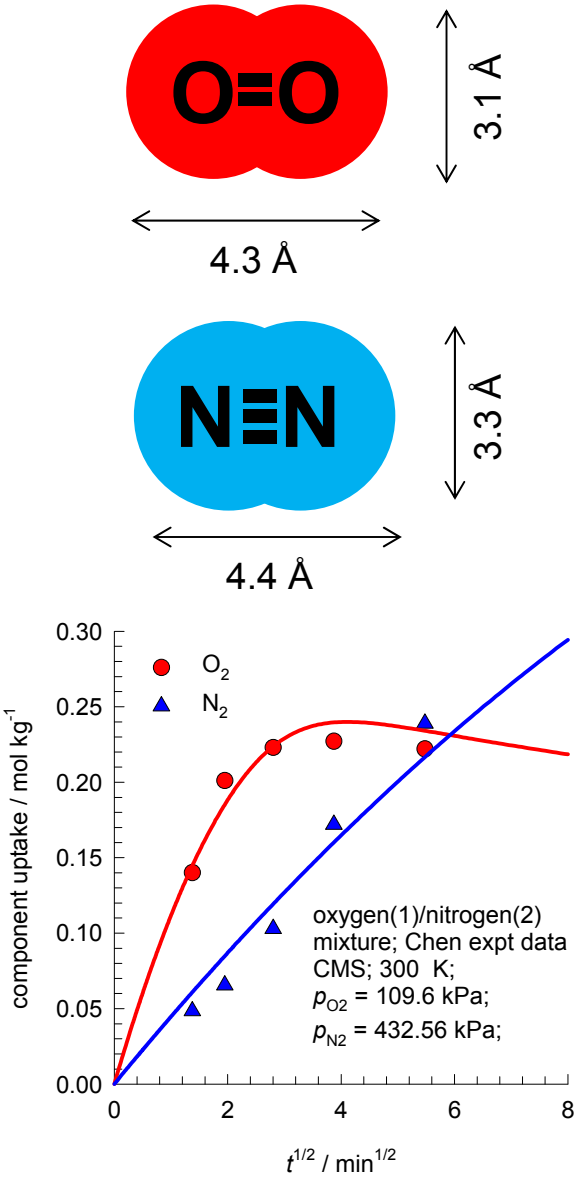
O=O
3.1 Å
4.3 Å
N≡N
3.3 Å
4.4 Å
0.30
0.25
0.20
0.15
0.10
0.05
0.00
component uptake / mol kg-1
O2
N2
oxygen(1)/nitrogen(2)
mixture; Chen expt data
CMS; 300 K;
pO2 = 109.6 kPa;
pN2 = 432.56 kPa;
0
2
4
6
8
t1/2 / min1/2

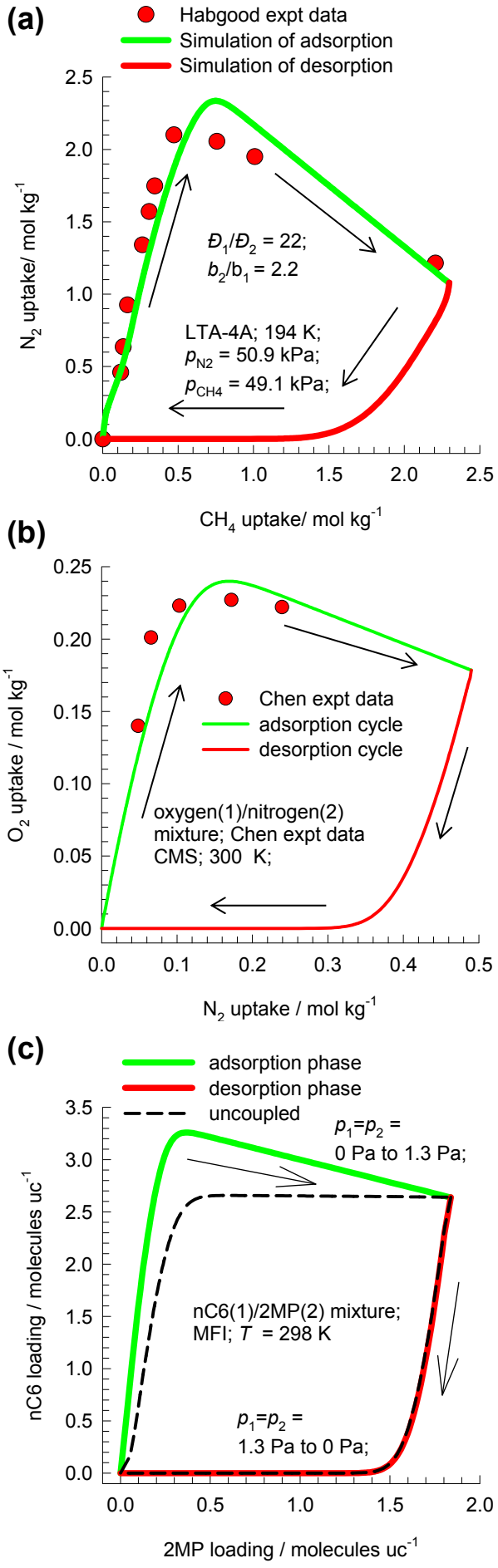
(a)
Habgood expt data
Simulation of adsorption
Simulation of desorption
$Đ_1/Đ_2$ = 22;
b_2/b_1 = 2.2
LTA-4A; 194 K;
p_{N2} = 50.9 kPa;
p_{CH4} = 49.1 kPa;
N_2 uptake/ mol kg^{-1}
CH_4 uptake/ mol kg^{-1}
(b)
Chen expt data
adsorption cycle
desorption cycle
oxygen(1)/nitrogen(2)
mixture; Chen expt data
CMS; 300 K;
O_2 uptake / mol kg^{-1}
N_2 uptake / mol kg^{-1}
(c)
adsorption phase
desorption phase
uncoupled
p_1=p_2 =
0 Pa to 1.3 Pa;
nC6(1)/2MP(2) mixture;
MFI; T = 298 K
p_1=p_2 =
1.3 Pa to 0 Pa;
nC6 loading / molecules uc^{-1}
2MP loading / molecules uc^{-1}

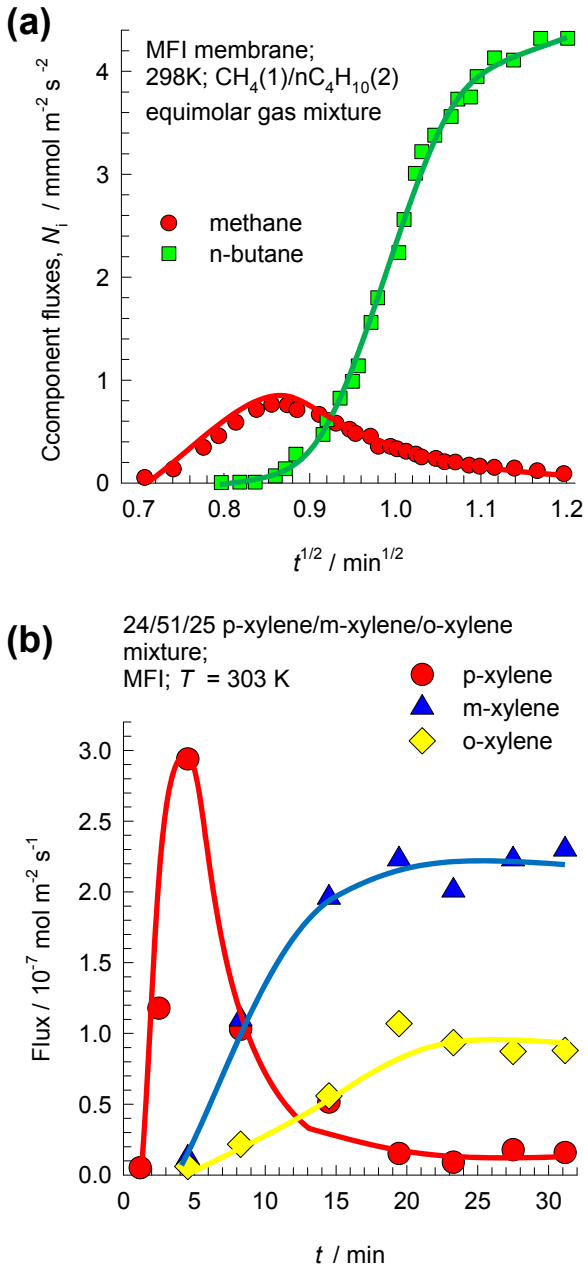
(a)
MFI membrane;
298K; CH4(1)/nC4H10(2)
equimolar gas mixture
methane
n-butane
Ccomponent fluxes, Ni / mmol m-2 s-2
t1/2 / min1/2
(b)
24/51/25 p-xylene/m-xylene/o-xylene
mixture;
MFI; T = 303 K
p-xylene
m-xylene
o-xylene
Flux / 10-7 mol m-2 s-1
t / min